1-1-2008

Temperature and silicon effects on tensile and corrosion behavior of chronium-molybdenum steel

Hanumantha Rao Chava
University of Nevada, Las Vegas

TEMPERATURE AND SILICON EFFECTS ON TENSILE AND CORROSION BEHAVIOR OF 9Cr-1Mo STEEL

by

Hanumantha Rao Chava

Bachelor of Engineering in Mechanical Engineering
Andhra University, Visakhapatnam, India
March 2004

A thesis submitted in partial fulfillment
of the requirements for the

Master of Science in Mechanical Engineering
Department of Mechanical Engineering
Howard R. Hughes College of Engineering

Graduate College
University of Nevada, Las Vegas
December 2008

UNLV
UNIVERSITY OF NEVADA LAS VEGAS

Thesis Approval

The Graduate College
University of Nevada, Las Vegas

November 26, 2008

The Thesis prepared by

Hanumantha Rao Chava

Entitled

Temperature and Silicon Effects on Tensile and Corrosion Behavior of 9Cr-1Mo Steel

is approved in partial fulfillment of the requirements for the degree of

Master of Science in Mechanical Engineering

Examination Committee Chair

Dean of the Graduate College

Examination Committee Member

Examination Committee Member

Graduate College Faculty Representative

ABSTRACT

Temperature and Silicon Effects on Tensile and Corrosion Behavior of 9Cr-1Mo Steel

by

Hanumantha Rao Chava

Dr. Ajit K. Roy, Examination Committee chair
Professor of Mechanical Engineering
University of Nevada, Las Vegas

Dr. Dr. Brendan O'Toole, Examination Committee chair
Associate Professor of Mechanical Engineering
University of Nevada, Las Vegas

Martensitic P91 grade steels containing 0.48, 0.96, 1.28 and 1.77 weight percent (wt%) silicon (Si) have been tested for evaluation of their tensile properties at temperatures ranging from ambient to 550 °C. The effect of activation using accelerator-driven electron beams on the room-temperature tensile properties of steels containing 0.48 and 1.28 wt% Si has also been investigated. The results indicate that all four heats of steel exhibited dynamic strain ageing at temperatures up to 400 °C. The activated specimens showed enhanced tensile strength but reduced ductility with increasing activation time, indicating radiation hardening of the tested materials. The electrochemically-polarized specimens showed more noble critical pitting potentials with increasing Si content due to the formation of more protective oxide films. While the tensile specimens tested at 550

^{o}C exhibited ductile failures, brittle failures were seen at ambient temperature. However, all activated specimens revealed cleavage facets, indicating predominantly brittle failures.

TABLE OF CONTENTS

LIST OF TABLES

LIST OF FIGURES

ACKNOWLEDGEMENTS

This work would not have been possible without the never-ending, untiring support of Professor Ajit K. Roy. During my last two years of stay at UNLV, Dr. Roy's unswerving support and guidance throughout the course of this research is gratefully acknowledged.

I would like to thank Dr. Doug Wells for his help in this project. I would also like to thank my committee members, Dr. Anthony Hechanova, Dr. Brendan O'Toole and Dr. Edward Neumann, for their direct and indirect contribution throughout this investigation. Special thanks goes to my friends Joydeep, Hasan, sudin, for their consistent help throughout my degree.

Without the long-distance love of my family – my father Mr. Ramaiah, my mother Mrs. Guna Sundari, my brothers Koteswara Rao and Suresh, sisters Krishna Veni and Anitha, and brother-in-law Revanth, I would not have been able to attend or complete Grad School. I offer them this Thesis in return for their sacrifices, and for sustaining me through the peaks and troughs of this process.

Finally I would like to acknowledge the financial support of the United States Department of Energy (USDOE).

CHAPTER 1

INTRODUCTION

The Yucca Mountain site located near Las Vegas, Nevada has been proposed to contain spent nuclear fuel (SNF) generated from nation's nuclear power plant, and defense high level waste (HLW). Even though this geologic repository may be capable to accommodate a significant amount of existing SNF/HLW, a large amount of radioactive waste is still being generated from current nuclear power plants, which may necessitate the development of additional disposal sites. In order to circumvent the problems associated with the disposal of future SNF/HLW, the United States Department of Energy (USDOE) has been considering different methods to either minimize or eliminate radioactive species from SNF so that they can be efficiently stored in the proposed Yucca Mountain repository for shorter durations without developing new disposal sites.

One method of minimizing or eliminating radioactive species from SNF is transmutation, which involves transformation of long-lived radioactive isotopes to species with relatively short half-lives and reduced radioactivity through capture and decay of minor actinides (MA) and fission products (FP). In this process, a target material, such as molten lead-bismuth-eutectic (LBE), is bombarded with accelerator-generated protons, thus generating neutrons. These neutrons are then impinged upon SNF/HLW, thereby producing MA and FP from SNF, as illustrated in Figure 1. These products will eventually be separated by a different method

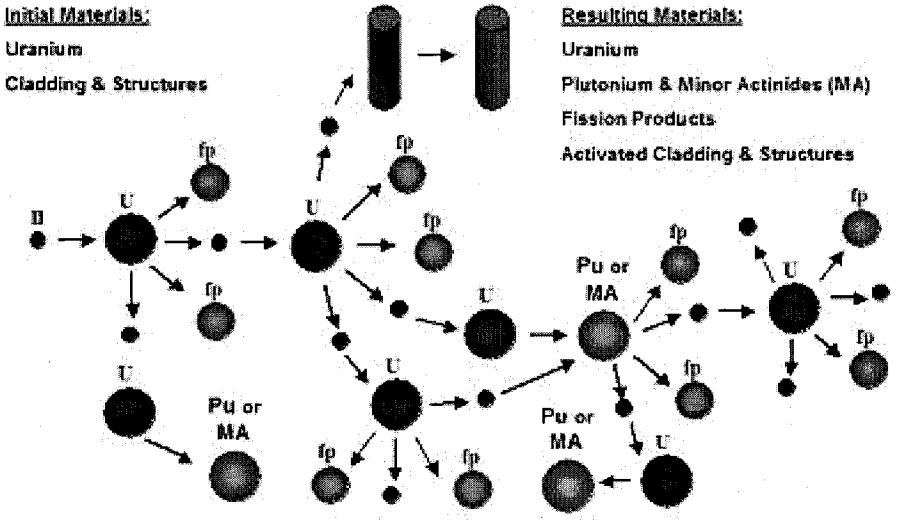

Figure 1-1. Production of Fission Products and Minor Actinides

The target material used in the transmutation process[1] will be contained inside a subsystem structure made of a suitable metallic material, such as martensitic stainless steel containing 9 wt% chromium (Cr) and 1 wt% molybdenum (Mo) in an iron (Fe) matrix, which is also known as 9Cr-1Mo steel. This type of steel has recently been modified through addition of niobium (Nb) and vanadium (V) [2] to enhance its high temperature metallurgical and mechanical properties. The modified 9Cr-1Mo steel possesses high tensile strength and reduced susceptibility to fatigue, thermal shock, void soiling, irradiation creep and high temperature helium embrittlement[3].

During the neutron generation process, also known as spallation, temperature ranging between 425 and 550 ^{0}C may be developed within molten LBE. Thus, the containment material used in the transmutation process must sustain elevated temperatures that may cause temperature-induced tensile deformation and environment-assisted degradations. Numerous studies, previously preformed [4] at UNLV's Material Performance Laboratory

(MPL), have exhibited a beneficial effect of silicon (Si) on both the tensile properties and the corrosion behavior of modified 9Cr-1Mo steel. In view of this rationale, the metallurgical and corrosion properties of this alloy have been evaluated in this investigation as a function of the Si content.

The modification of 9Cr-1Mo steel through addition of Nb and V has been aimed at enhancing its tensile strength, thermal conductivity and corrosion resistance, and reducing its thermal expansion. This grade of Cr-Mo stainless steel, commonly known as either the T91 or P91 grade steel, has recently been proposed for applications in the window separating the accelerator area from the liquid metal spallation target, and the target container in the accelerator-driven-systems (ADS). The identification of modified 9Cr-1Mo steels either as T91 or P91 grade steel is based on their product form. Tubular and plate materials of this type of steel are designated by T91 and P91, respectively. These alloys are commonly used in the quenched and tempered conditions, which can lead to the formation of fine-grained tempered martensitic microstructure that may provide a combination of excellent tensile strength and ductility. Because of the high hardenability, the tempered martensitic microstructure can provide excellent strength and toughness in T91 / P91 grade steels. Thus, this grade of steel becomes a suitable candidate structural material for use in the temperature regime of 400-600 ^{0}C, which is also very similar to the operating temperature range proposed for the spallation process.

In order to study the role of Si content on the performance of P91 grade steel for transmutation application, four experimental heats of modified P91 grade steel having different levels (0.48, 0.96, 1.28 and 1.77 wt. %) of Si content were custom-melted by a vacuum-induction-melting (VIM) practice at the Timken Research Laboratory (TRL).

These VIM heats of martensitic steels were subsequently forged, hot-rolled and heat treated to develop the desired metallurgical microstructure prior to the fabrication of test specimens.

The structural material containing the molten LBE may also undergo radiation-hardening during the spallation process, leading to enhanced tensile strength but unusually reduced ductility. Therefore, P91 grade steels of different Si content were subjected to radiation by using accelerator-based irradiation. The specimens were activated for different time periods, and following radioactive decay they were tested for evaluation of their tensile properties. Limited studies were also performed to evaluate the localized (pitting and crevice) corrosion behavior of P91 grade steel in an acidic solution as a function of the Si content. Thus, in essence, this thesis presents the comprehensive test results on the role of Si content on the tensile properties of P91 grade steel, with and without irradiation, and its localized corrosion susceptibility in a hostile aqueous environment.

CHAPTER 2

TEST MATERIALS AND SPECIMENS

2.1 Test Materials

Martensitic Cr-Mo steels, such as P91 grade steels, have been widely used in aerospace, general engineering and nuclear applications. The superior performance of these types of steel, compared to that of austenitic alloys, can be attributed to their stable metallurgical microstructures, high oxidation and sulfidation resistance, improved thermal conductivity, and low thermal expansion. These materials are known to have a body-centered-tetragonal (BCT) structure in the hardened state. The typical mechanical and physical properties of P91 grade steels at ambient temperature are given in Tables 2-1 and 2-2, respectively.

Table 2-1 Tensile Properties of Modified 9Cr-1Mo Steel

Ultimate Tensile Strength (UTS)	85 ksi (586 MPa), minimum
Yield Strength (YS)	60 ksi (414 MPa), minimum
% Elongation (%El)	20, minimum
% Reduction in Area (%RA)	40, minimum
Hardness	248 H_B, minimum

Table 2-2 Physical Properties of P91 Grade Steel

Density	7.6 gm/cc
Thermal Conductivity (λ)	27 $W.m^{-1}.K^{-1}$
Electrical Resistivity (ρ)	$55x10^{-8}$ $\Omega.m$

As the title of this investigation implies, the primary objective was to study the effect of Si content on both the tensile properties and corrosion resistance P91 grade steels. Therefore, four experimental heats of this type of steel were custom-melted at the Timken Research Laboratory using a vacuum-induction-melting (VIM) practice. The VIM heats were subsequently forged and hot-rolled, followed by thermal treatments. The ingots were forged at 1204 °C into billets and air-cooled. The billets were then rolled at an identical temperature into plates of different dimensions, followed by air-cooling. Subsequently, these plates were austenitized at 1100 °C for 1 hour and oil quenched. The quenched plates were then tempered at 621 °C for an hour, followed by air-cooling. The chemical compositions of all four heats of P91 grade steel are given in Table 2-3.

Table 2-3 Chemical Compositions of Tested Materials

Heat No.	Elements (wt %)												
	C	Mn	P	S	Si	Ni	Cr	Mo	Al	V	Cb	N	Fe
2525	.11	.46	.004	.004	.48	.31	9.06	1.05	.018	.24	.91	65	Bal
2523	.11	.46	.004	.004	.96	.31	9.13	1.02	.031	.22	.89	53	Bal
2526	.12	.45	.004	.004	1.28	.31	9.11	1.02	.024	.22	.085	66	Bal
2425	.10	.45	.005	.000	1.77	.31	9.03	1.05	.028	.24	.087	30	Bal

2.2 Test specimens

2.2.1 Tensile specimen

Smooth cylindrical specimens having 4-inch (101.4 mm) overall length, 1-inch (25.4 mm) gages length and 0.25-inch (6.35 mm) gage diameter were machined from the heat-treated plate materials of different heats in such a way that the gage-section was parallel to the longitudinal rolling direction. A gage length (l) to gage diameter (d) ratio (l/d) of 4 was maintained for these specimens to comply with the size requirements of the ASTM Designation E 8. [5] The detailed dimensions and a pictorial view of the cylindrical specimens used in the evaluation of room-temperature tensile properties, with and without irradiation, are shown in Figure 2.1. These specimens were also used to determine their tensile properties at elevated temperatures without the radiation effect as a function of Si content

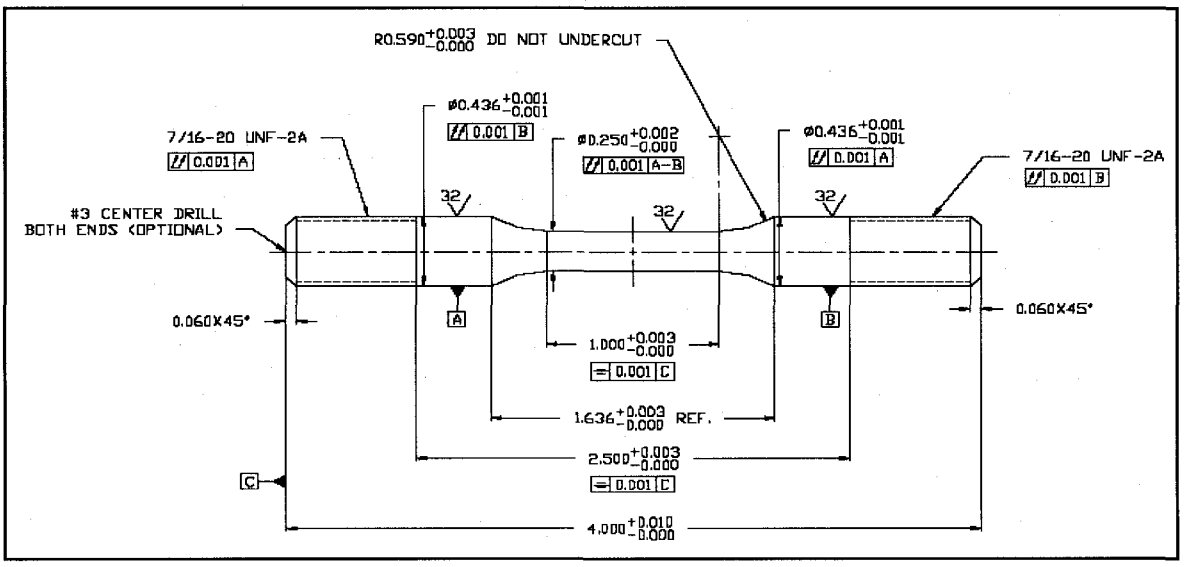

(a) Dimensions (in inches)

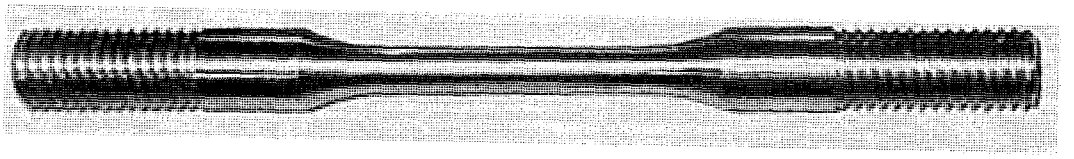

(b) Pictorial View

Figure 2.1 Tensile Specimen

2.2.2 Polarization Specimen

Cylindrical specimens having 0.5-inch (12.7-mm) length and 0.375-inch (9.5-mm) diameter were used to evaluate the localized corrosion behavior of P91 grade steels using an electrochemical polarization technique. The dimensions and a pictorial view of the polarization specimen are illustrated in Figure 2.2.

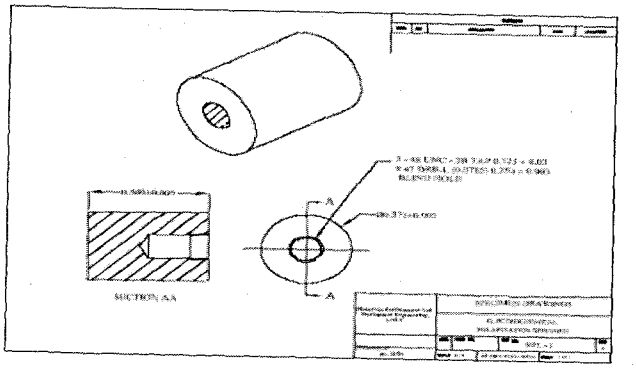

(a) Dimensions (in inches)

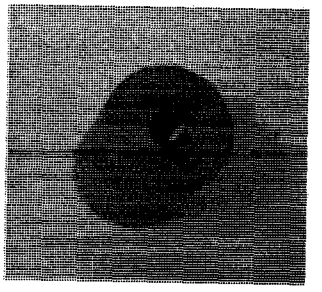

(b) Pictorial view

Figure 2.2 Polarization Specimen

CHAPTER 3

EXPERIMENTAL PROCEDURES

This investigation is focused on the evaluation of the tensile properties of P91 grade steels with different Si content, at ambient and elevated temperatures (up to 550^0C). The tensile properties of a few selected P91 grade steels, activated with electron beams from a 25 MeV linear accelerator, have also been determined at ambient temperature. A limited number of electrochemical polarization testing has been performed to determine the corrosion susceptibility of the alloys at ambient temperature. Further, metallographic and fractographic evaluations have also been performed to determine the metallurgical microstructures of the tested materials, and the fracture morphology of all tested specimens.

3.1 Tensile Properties Evaluation

The tensile properties of P91 grade steels of different Si content including, The yield strength (YS), The ultimate tensile strength (UTS), and the ductility in terms of percent elongation (%EI) and percent reduction in area (%RA) were evaluated using smooth cylindrical specimens, with and without irradiation. Instron model 8862 testing equipment (Figure 3.1) was used for evaluation of the tensile properties at temperatures ranging from ambient to 550^0C. The specimens were loaded in tension at a strain rate of 5×10^{-4} sec^{-1} according to the ASTM Designation E 8-2004. The experimental data

including the load, time, extension, engineering stress and engineering strain were recorded in the data file. Duplicate specimens were tested under each experimental condition, and the average values of the measured parameters were recorded. The engineering stress versus engineering strain (s-e) diagrams were automatically generated using the Bluehill 2 software program [6] that enabled the data acquisition during entire testing period. The magnitudes of YS, UTS, and %EI based on the linear-variable-displacement-transducer (LVDT) measurements at each temperature, were also evaluated using this software. The magnitude of YS was determined from the point of intersection of a line drawn parallel to the linear portion of the s-e diagram at a strain offset value equivalent to 0.2% of the strain. Upon completion of testing, the magnitudes of %EI and %RA were also calculated using Equations 3-1 through 3-4.

$$\%\ \mathrm{El} = \left(\frac{L_f - L_o}{L_g}\right) \times 100 \quad ; \quad L_f > L_o \qquad \text{Equation 3-1}$$

$$\%\mathrm{RA} = \left(\frac{A_o - A_f}{A_o}\right) \times 100 \; ; \quad A_o > A_f \qquad \text{Equation 3-2}$$

$$A_o = \frac{\pi \times D_o^{\,2}}{4} \qquad \text{Equation 3-3}$$

$$A_f = \frac{\pi \times D_f^{\,2}}{4} \qquad \text{Equation 3-4}$$

A_0 = Initial cross sectional area ($inch^2$)

A_f = Cross sectional area at failure ($inch^2$)

L_o = Initial overall length (inch.)

L_f = Final overall length (inch.)

D_o = Initial gage diameter (inch.)

D_f = Final gage diameter (inch.)

The Instron testing machine, shown in Figure 3-1, had an axial load transducer capacity of 22.5 kip (100 kN). It had a single screw electromechanical top actuator that was developed for static and quasi-dynamic cyclic testing at slow speeds. This equipment consisted of a large heavy-duty load frame with an adjustable crosshead attached to the top grip, and a movable actuator with another grip at the bottom to enable loading and unloading of the test specimen. The axial motion was controlled by force, displacement, or an external signal from the strain gage. The specimen was mounted between two grips and pulled by the movable actuator. The load cell measured the applied force on the tensile specimen. The movement of the upper crosshead relative to the lower one measured the strain within the specimen. The key specifications of the Instron equipment are given in Table 3-1. [7]

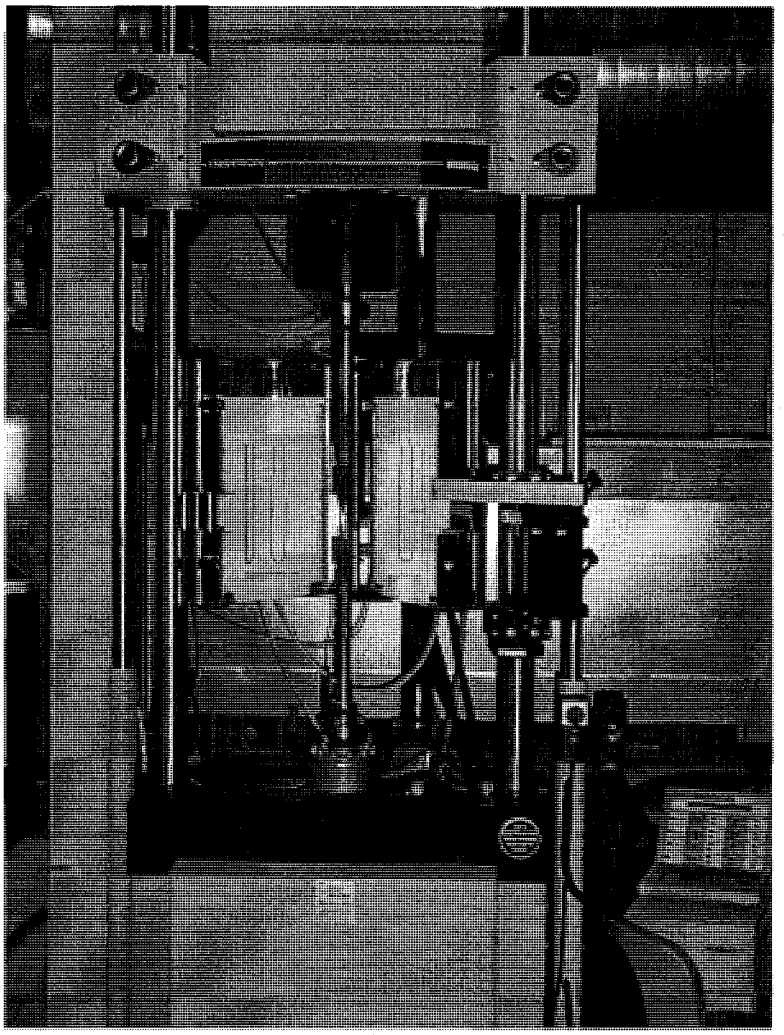

Figure 3-1 Instron Testing Machine

Table 3-1 Specifications of Instron Model 8862 System

Load Capacity, kN	Total Actuator Stroke, mm	Maximum Ramp Rate, mm/min	Actuator Attachment Threads	Load Cell Attachment Threads
100	100	350	M30 × 2	M30 × 2

A Split furnace (MDS 1735A) was attached to the Instron machine for heating the test specimens at the desired temperatures in the presence of nitrogen. This furnace was capable of sustaining a maximum temperature of 1500 ^{0}C, and consisted of two water-cooled stainless steel jackets that provided a safe ergonomic outer surface for operation. Two layers of micro-pores and ceramic fibers were placed inside this furnace. Six U-shaped molybdenum disilicide heating elements were used for attaining the desired testing temperature. The testing temperature was monitored by three B-type thermocouples contained inside the ceramic test chamber. A separate control panel (model-CU666F) was used to perform the overall monitoring of temperature during tensile loading. This control panel had a capability of heating at a maximum rate of 10 ^{0}C per minute. However, a slower heating rate of 4 ^{0}C per minute was used during tensile testing to prevent any thermal shock to the pull rods and the fixtures inside the furnace. Since the grip material could undergo plastic deformation and phase transformation at elevated temperatures during straining, a pair of custom-made grips made of high strength and temperature resistant MarM 246 alloy was used to hold the tensile specimen in an aligned position. A positive pressure was maintained inside the heating chamber by continuously purging nitrogen through it, which also ensured the elimination of oxygen from the test camber, thus preventing contamination of the specimen surface at elevated temperatures.

3.2 Tensile Testing of irradiated Specimens

Smooth cylindrical specimens, having dimensions similar to that of the tensile specimens described earlier, were irradiated by using electron beams from a 25 MeV

Linear Accelerator (LINAC) [8] at the Idaho Accelerator Center of the Idaho State University. These specimens were subjected to electron beam radiation for periods of 2, 4, 6 and 8 hours. The average dose rate resulting from the irradiation process, and the associated details are given in Table 3.2. The experimental setup used during the irradiation process is shown in Figure 3.2. Subsequent to the irradiation process, these specimens were allowed to reduce their radiation levels (i.e., half-lives) so that they could be handled safely for further tensile testing at ambient temperature using the Instron equipment. Tensile properties including YS, UTS, %El and %RA of the activated specimens were then evaluated as a function of the dose rate and the Si content.

Table 3.2 Specification of Electron Beam

Sample Distance	Pulse Width	Repetition Rate	Energy	Pick up Loop Signal
40 cm	4 S	60 Hz	22 MeV	60 mA

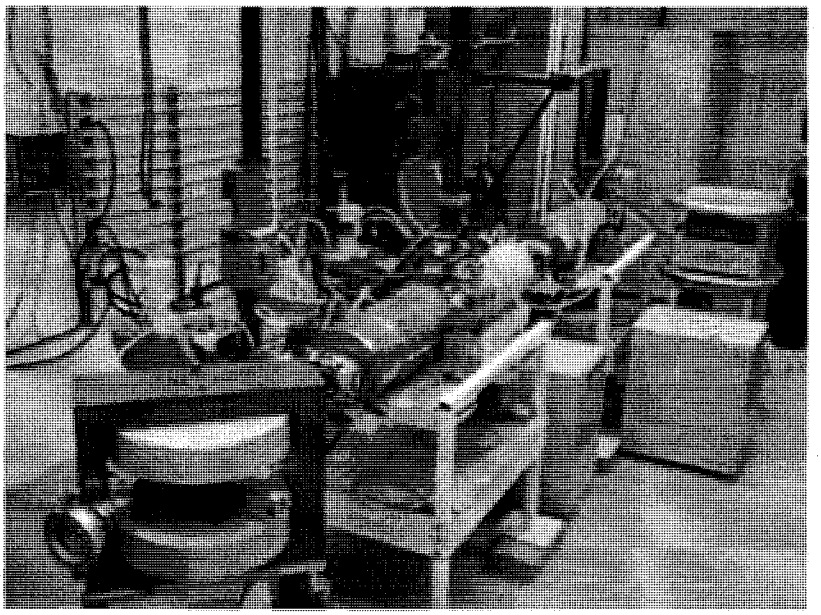

Figure 3.2 LINAC Setup for irradiation

3.3 Localized Corrosion Study

The susceptibility of the P91 grade steels of different Si content to pitting and crevice corrosion was determined by performing cyclic potentiodynamic polarization (CPP) experiments in an acidic aqueous solution (pH~2.2) using a Gamry potentiostat. The CPP testing was based on a three-electrode polarization concept, in which the working electrode (specimen) acted as an anode and two graphite electrodes (counter electrodes) acted as cathodes. The reference electrode was made of silver/silver chloride (Ag/AgCl) solution contained inside a Luggin probe having the test solution that also acted as a salt bridge. The CPP test setup is shown in Figure 3.3. The tip of the Luggin probe was placed within a distance of 2 to 3 mm from the test specimen, as shown in Figure 3.4.

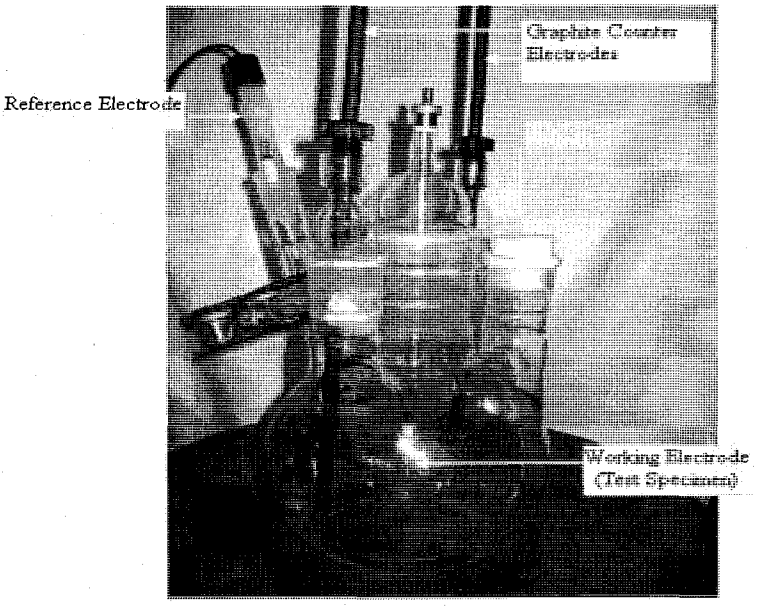

Figure 3.3 CPP Test Setup

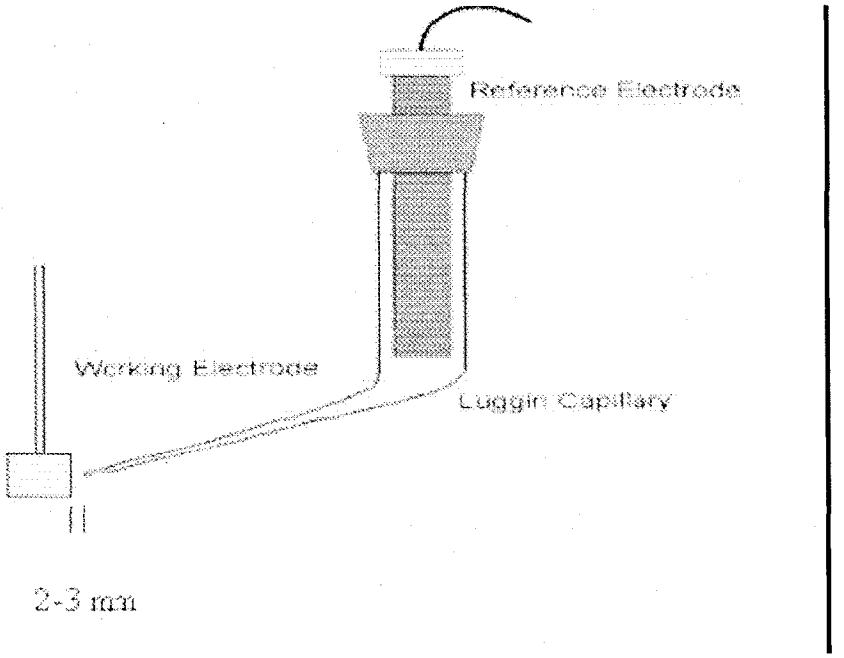

Figure 3.4 Luggin Probe Arrangement

The potentiostat was calibrated according to the ASTM Designation G 5 [9] prior to the performance of the CPP experiments. This standard dictates that the resultant polarization diagram must exhibit a pattern similar to that shown in Figure 3.5, which can be generated when Type 430 ferritic stainless steel is subjected to potentiodynamic polarization in an 1N (1 Normal) H_2SO_4 solution at 30 ^{0}C. The CPP experiment was performed using a small cylindrical specimen, a configuration of which has been shown in the previous chapter. The corrosion or open circuit potential (E_{corr}) of this specimen was initially determined by immersing it in an acidic solution for approximately 50 minutes, followed by acanning of potential in the forward and reverse direction at a rate of 0.17mv/see. [10] The magnitudes of other critical potentials such as the critical pitting potential (E_{pit}) and the protection potential (E_{port}), if any, were determined from the resultant CPP diagram (potential versus log current density plot).

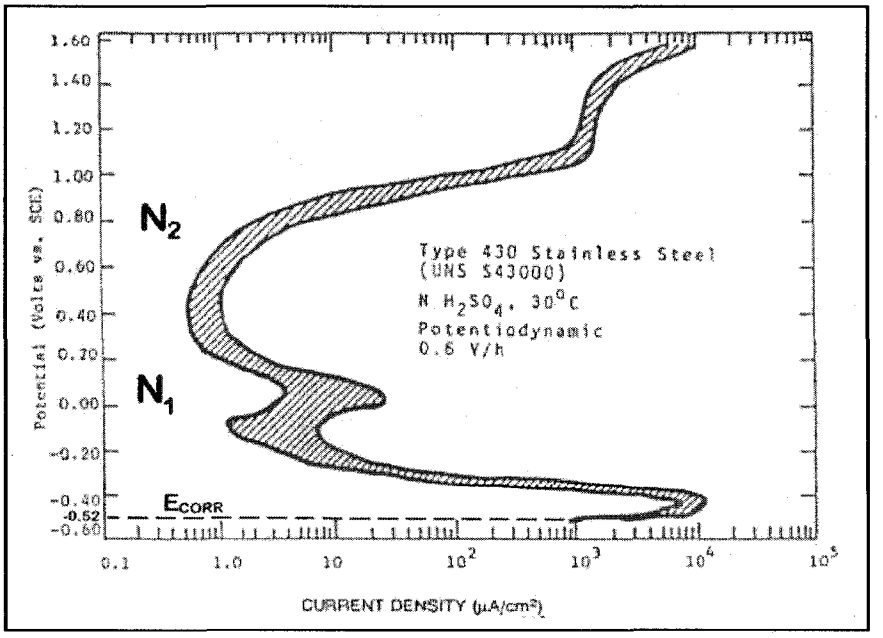

Figure 3.5 ASTM G 5 Potentiodynamic Polarization Diagram

3.4 Optical Microscopy

Microstructure plays an important role in differentiating properties of one alloy versus other. Thus, the evaluation of metallurgical microstructures constitutes a significant step in characterizing the performance of a material of interest. For microstructural evaluations, it is customary to prepare the specimen surface with high precision. Thus, the following method was used to prepare the specimen surface.

The specimens were mounted using the right ratio of epoxy and hardener. The mounted specimens were ground with rotating discs containing the abrasive papers. The grinding procedure involved several stages using a finer paper each time. The sample was oriented perpendicular to the previous scratches after every step. The polished sample was then washed with deionized water to prevent any contamination, and dried with ethanol. Finally, etching was done using 5% Nital and Beraha's reagent. 5% Nital is a common etchant for steels that can reveal ferrite grain boundaries and martensites. Beraha's reagent can preferentially attack the ferrite grain boundaries and color them. [11] The polished and etched samples were then subjected to microstructural evaluations using a Leica optical microscope (Figure 3-6), which had a maximum magnification of 1000X. A digital camera with a resolution of 1 mega pixel enabled image capture on a computer screen utilizing software provided by Leica.

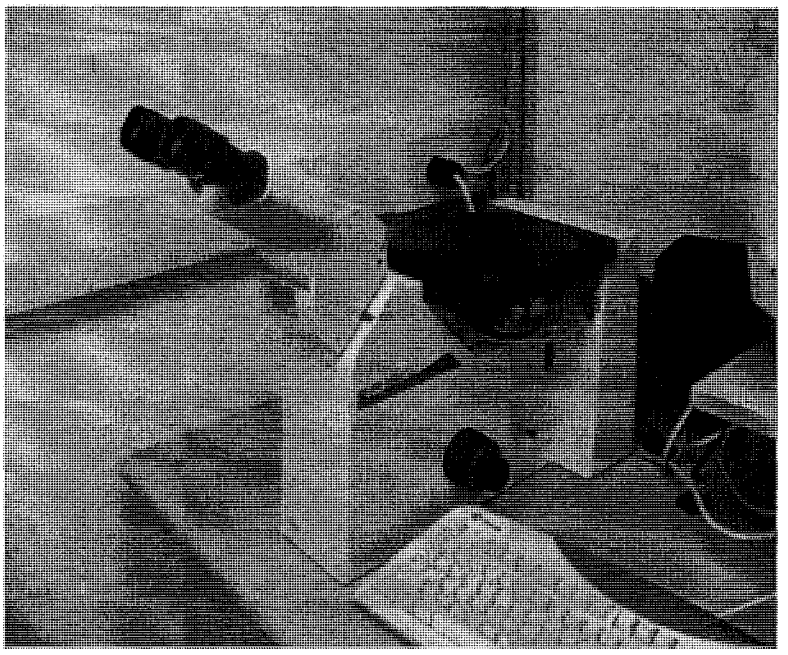

Figure 3-6 Leica Optical Microscope

3.5 Fractographic Evaluations

The extent and morphology of failure of the tested specimens were determined using a Jeol-5600 scanning electron microscope (SEM), shown in Figure 3-7. The tested specimens were sectioned into ½ to ¾ of an inch in length to accommodate them in a vacuum chamber of the SEM. Failures can usually be classified into two major types including ductile and brittle.[12] Dimpled microstructure is a characteristic of ductile failure. On the other hand, brittle failures may exhibit intergranular and transgranular cracking depending on the tested materials.

In SEM evaluations, electrons from a metal filment are collected and focused similar to light waves into a narrow beam. The beam scans across the subject, which is synchronized with a spot on a computer screen. Electrons scattred from the subject are detected and can create a current, the strength of which makes the spot on the computer

brighter or darker. This current can create a photograph-like image with an exceptional depth of field. Magnification of several thousands can be achieved by use of SEM.

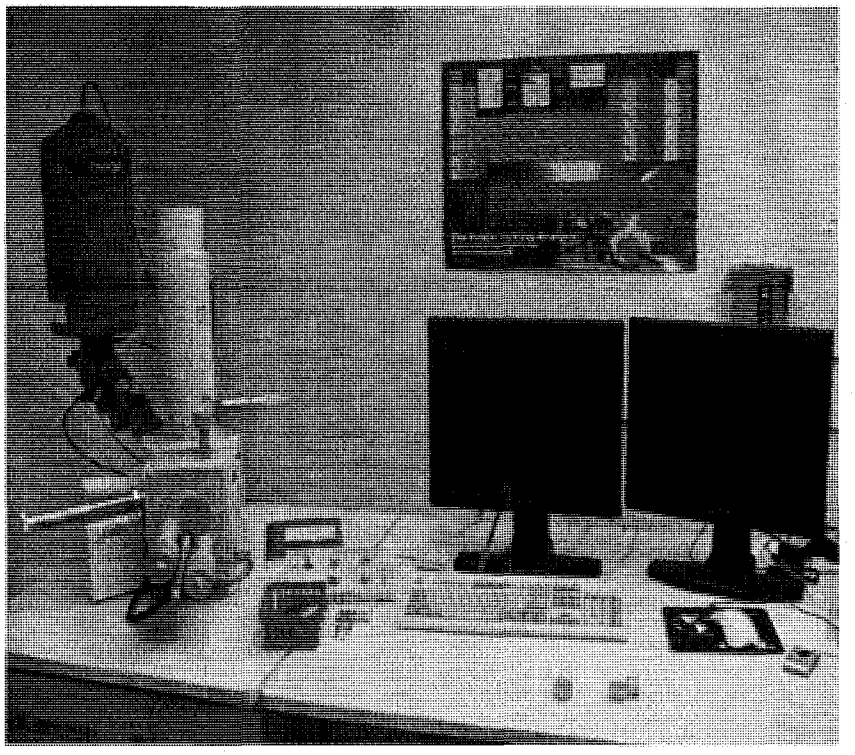

Figure 3-7 Jeol Scanning Electron Microscope

CHAPTER 4

RESULTS

This chapter presents the results of tensile testing of P91 grade steel of varied Si content as a function of temperature. In addition, the effect of irradiation on the resultant tensile properties of the tested materials has been presented. The results of limited electrochemical testing are also included. Further, the results of metallographic and fractographic evaluations of the tested specimens using different microscopic techniques have been discussed in detail.

4.1 Microstructural Evaluation

The optical micrographs of the polished and etched specimens of all four heats of P91 grade steel are shown in Figures 4-1 through 4-4. Steels containing 0.48 weight percent (wt%) Si was etched using both Nital and Beraha's reagent. On the other hand steels having 0.98, 1.28 and 1.77 wt% Si were etched in "Beraha's reagent". The compositions of these etchants are given in Table 4-1. An evaluation of these micrographs revealed austenitic grain boundaries containing finely dispersed martensites, as expected for quenched and tempered steels. Delta ferrites, oriented in different directions, were also visible throughout the martensitic structure due to the presence of high chromium content.

Table 4-1 Compositions of Etchants

Etchant	Composition	
Nital	50 ml Nitric acid	950 ml ethyl alcohol
Beraha's Reagent	10 grams $Na_2S_2O_3$ 3 grams $K_2S_2O_5$	100 ml H_2O

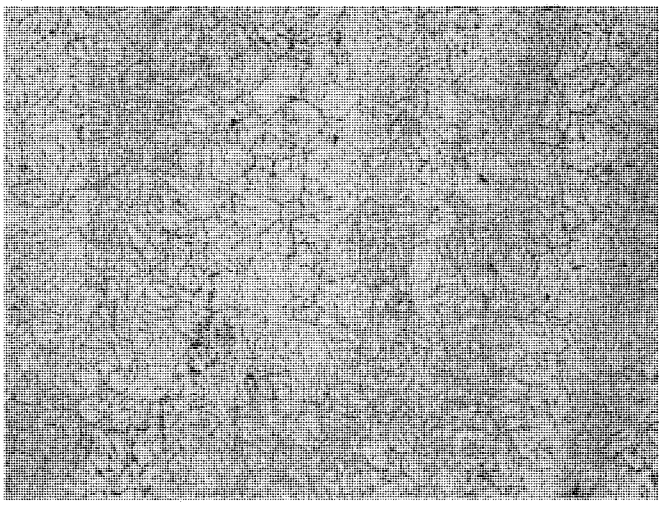

(a) Nital, 500X

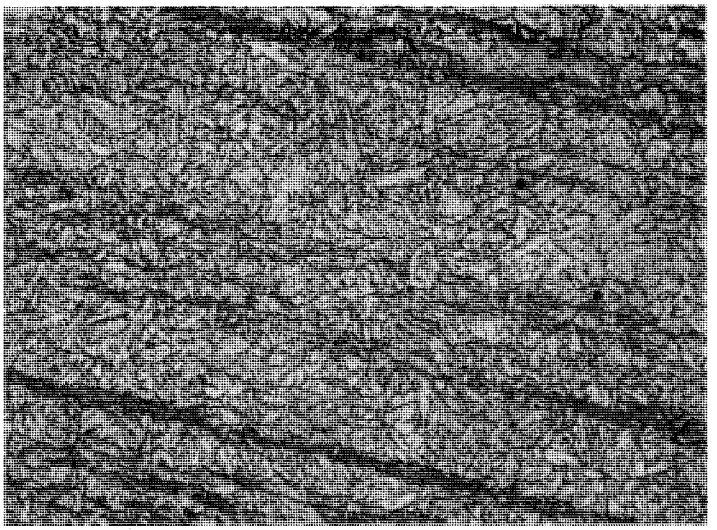

(b) Beraha's Reagent, 500X

Figure 4-1 Optical Micrographs of Steel with 0.48 wt% Si

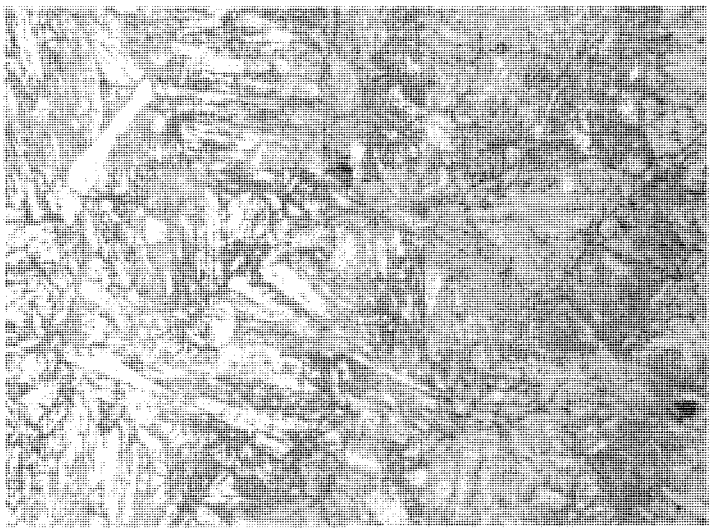

Figure 4-2 Optical Micrograph of Steel with 0.96 wt% Si, Nital Reagent

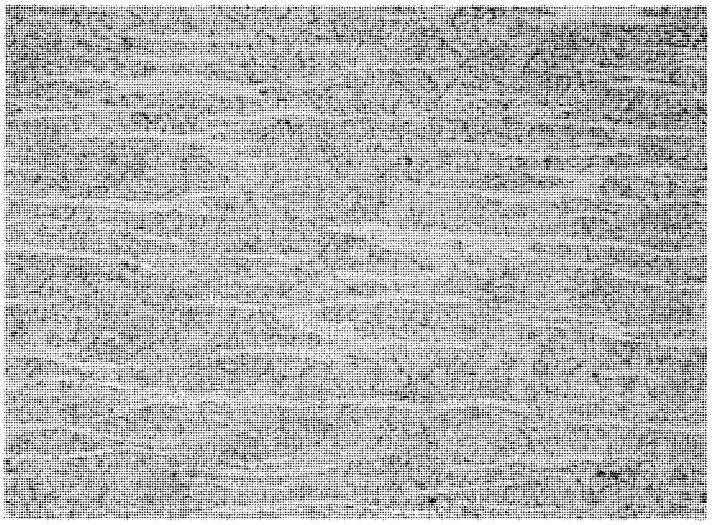

Figure 4-3 Optical Micrograph of Steel with 1.28 wt% Si, Beraha's Reagent

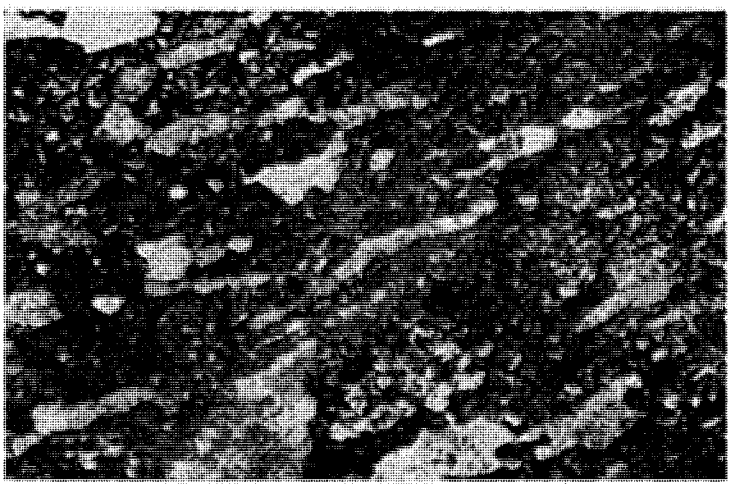

Figure 4-4 Optical Micrograph of Steel with 1.77 wt% Si, Beraha's Reagent

4.2 Tensile Properties without Irradiation

The results of tensile testing involving all four Si-containing P91 grade steels at temperatures up to 550 ^{0}C are illustrated in Figures 4-5 through 4-8 in the form of superimposed engineering stress versus engineering strain (s-e) diagrams. An evaluation of these diagrams reveals that, in general, the magnitude of failure strain (e_f) was

gradually reduced with an increase in temperature from ambient to 300 °C, irrespective of the Si content. Simultaneously, serrations were also seen in the s-e diagrams generated at ambient temperature, 150, 300, and 400 °C. The occurrence of reduced e_f and formation of serrations within certain temperature ranges is known [13-17] to be associated with a metallurgical phenomenon, termed dynamic strain ageing (DSA). A mechanistic understanding of DSA of iron-chromium-molybdenum (Fe-Cr-Mo) steels, based on the evaluations of parameters including dislocation density, irradiation energy, and work-hardening index, has recently been developed and published [18,19] by researchers at the Materials Performance Laboratory of UNLV. Therefore, no additional efforts have been made in this investigation to revisit this concept.

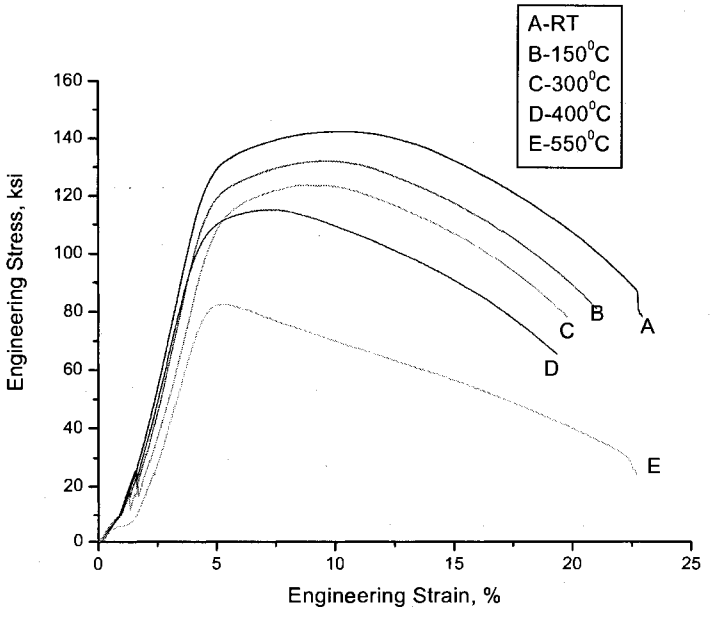

Figure 4-5 s-e Diagram vs. Temperature for Steel Containing 0.48 wt% Si

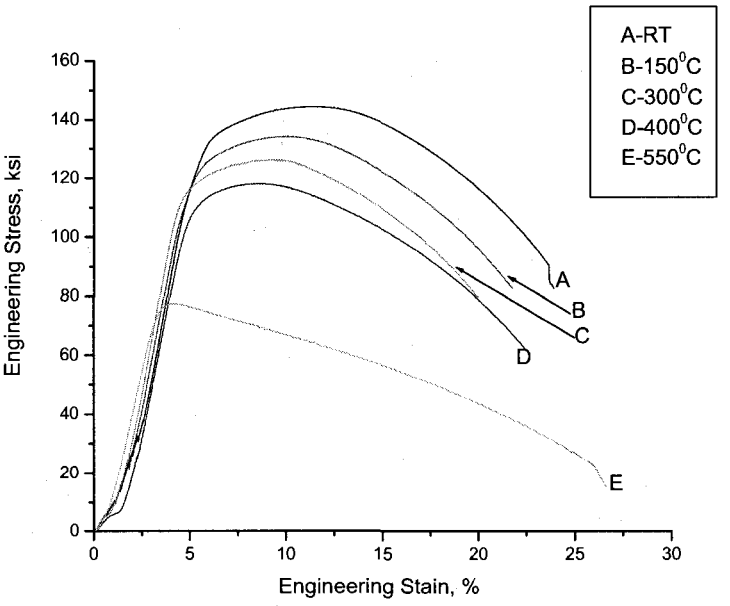

Figure 4-6 s-e Diagram vs. Temperature for Steel Containing 0.96 wt% Si

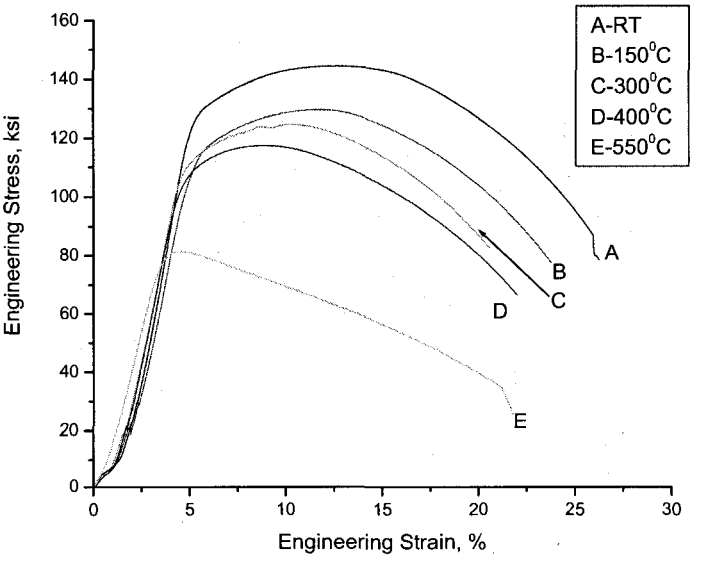

Figure 4-7 s-e Diagram vs. Temperature for Steel Containing 1.28 wt% Si

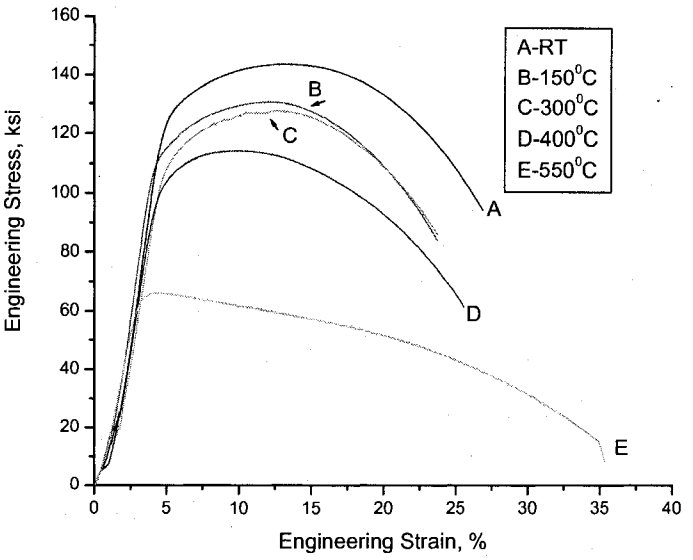

Figure 4-8 s-e Diagram vs. Temperature for Steel Containing 1.77 wt% Si

The average values of YS, UTS, %El and %RA (based on duplicate testing), determined from the s-e diagrams and the specimen dimensions, before and after testing, are given in Table 4-2. The variations of YS and UTS with temperature are illustrated in Figures 4-9 and 4-10, respectively as a function of the Si content. An examination of these data indicates that the magnitude of YS and UTS was gradually reduced with increasing temperature up to 400 °C, followed by their drastic drop at 550 °C. As to the effect of temperature on ductility, the magnitude of %El and %RA was gradually reduced with increasing temperature up to 300 °C. Beyond this temperature, both parameters were enhanced due to increased plasticity. The reduced ductility in terms of both %El and %RA at temperatures up to 300 °C was consistent with the occurrence of the DSA Phenomenon within this temperature regime. It should also be noted that the reduced tensile strength (YS and UTS) and greater ductility (%El and %RA) with increasing

temperature were more pronounced in the Fe-Cr-Mo steel containing the highest Si content (1.77 wt%)

Table 4-2 Tensile Properties vs. Temperature

Heat No./Si Content (wt%)	Temperature (°C)	Average YS (ksi)	Average UTS (ksi)	Average %El	Average %RA
2525/0.48	Ambient	128	143	23.7	69
	150	116	133	17.8	65.5
	300	109	124	17.4	65.5
	400	103	115	18.7	69
	550	79	83	23.5	82
2523 /.96	Ambient	128	145	22.8	69
	150	119	135	17.3	66.7
	300	110	127	17.4	66.7
	400	105	118	19.7	71
	550	73	78	27	85
2526 /1.28	Ambient	126	144	26	70.8
	150	111	130	21.7	71.4
	300	107	125	20.9	69.6
	400	102	117	21	74.4
	550	77	81	22	78
2425/1.77	Ambient	121	144	26.2	63.8
	150	108	131	22.1	65.5
	300	104	128	21.3	60
	400	96	114	24.4	73
	550	61	66	35.1	89

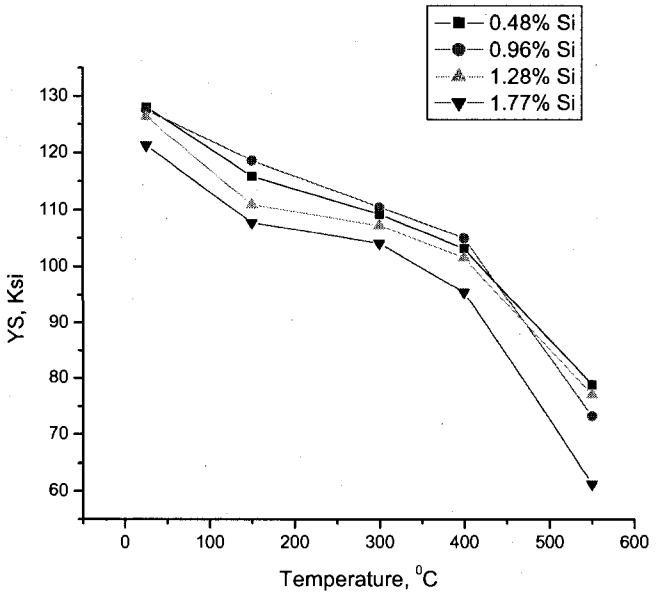

Figure 4-9 YS vs. Temperature

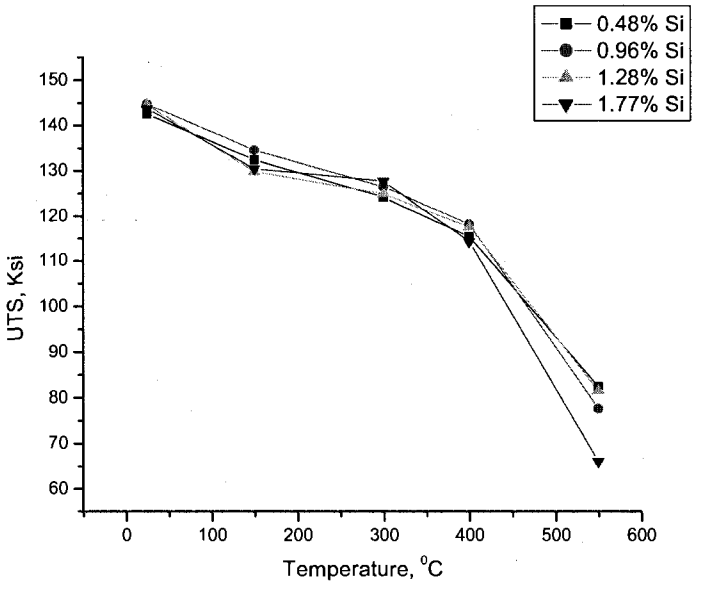

Figure 4-10 UTS vs. Temperature

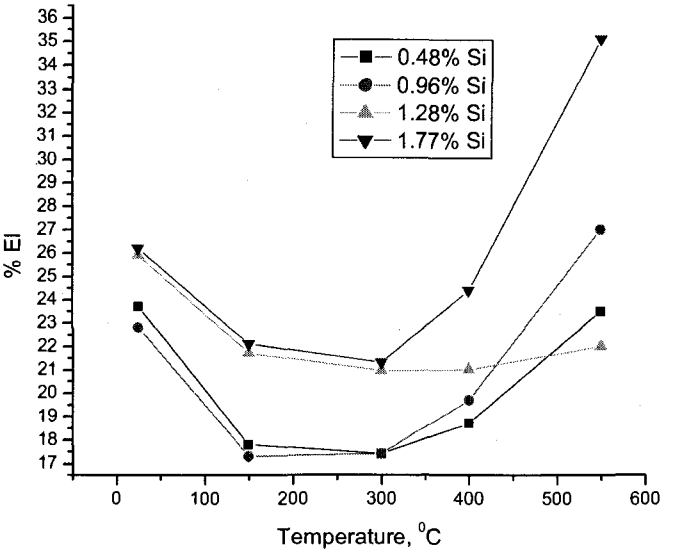

Figure 4-11 %El vs. Temperature

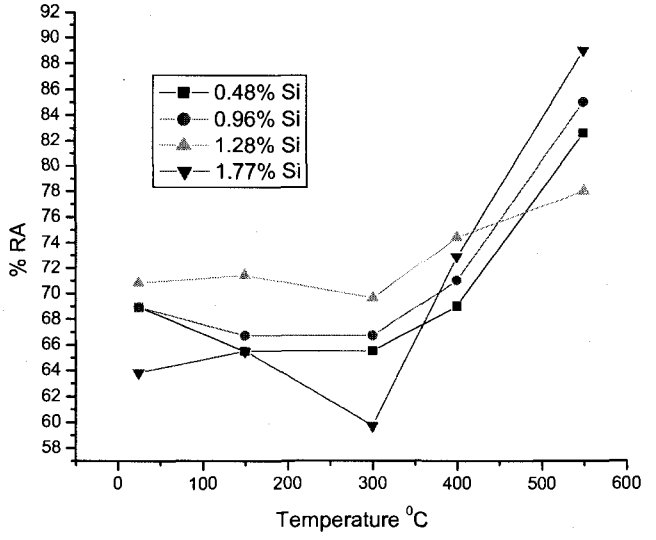

Figure 4-12 %RA vs. Temperature

4.3 Tensile Properties with Irradiation

The results of tensile testing involving irradiated smooth cylindrical specimens of P91 grade steels containing 0.48 and 1.28 wt% Si are illustrated in Figures 4-13 and 4-14, respectively. These plots show superimposed s-e diagrams generated at ambient temperature as a function of the irradiation time. The resultant tensile data including YS, UTS, %El and %RA are given in Table 4-3. An evaluation of these data indicates that, irrespective of the Si content, both alloys experienced hardening due to the irradiation process, showing gradually-enhanced tensile strength (YS and UTS) but reduced ductility (%El and %RA) with increased irradiation time. Such phenomenon of hardening is commonly referred to as radiation hardening.[20] The variations of all four parameters with irradiation time are illustrated in Figures 4-15 through 4-18, and Figures 4-19 through 4-22 for steels containing 0.48 and 1.28 wt% Si, respectively.

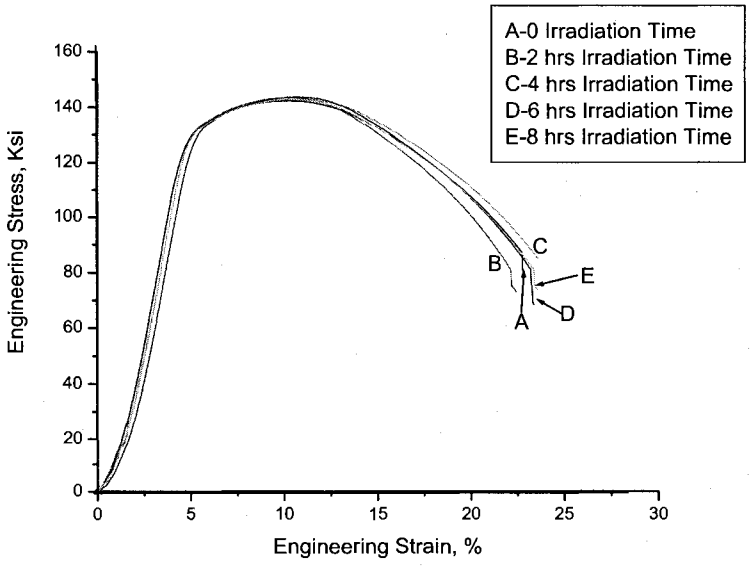

Figure 4-13 s-e Diagram of Steel with 0.48 wt% Si vs. Irradiation Time

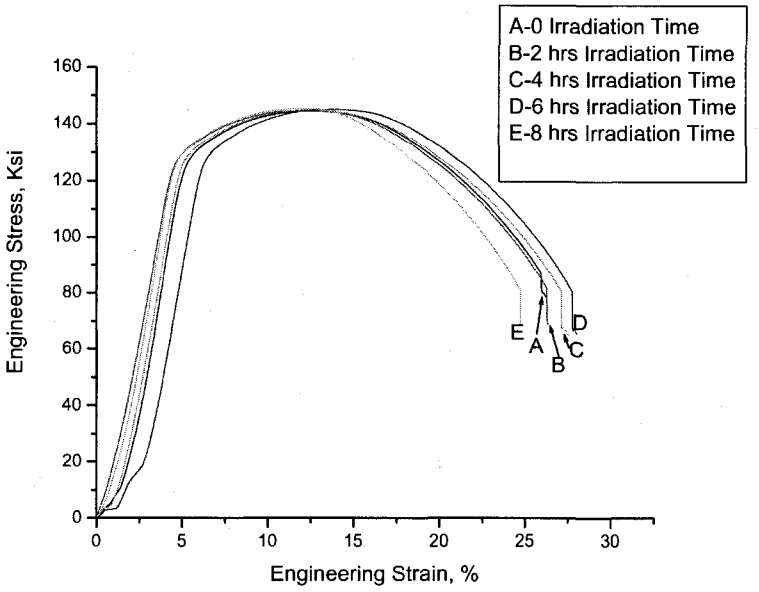

Figure 4-14 s-e Diagram of Steel with 1.28 wt% Si vs. Irradiation Time

Table 4-3 Results of Ambient-Temperature Tensile Testing using Irradiated Specimens

Heat No./Si Content (wt%)	Irradiation Time (hrs)	Average YS (ksi)	Average UTS (ksi)	Average %El	Average %RA
2525/0.48	0	126	142	22.8	68.9
	2	127	143	22.2	68
	4	128	144	21.7	67.4
	6	129	144	20.2	66.3
	8	130	145	19.6	65.2
2526/1.28	0	126	144	26.2	70.8
	2	127	145	25.8	68.8
	4	127	146	24.6	67.7
	6	127	146	23.2	66.5
	8	129	147	21.7	65.2

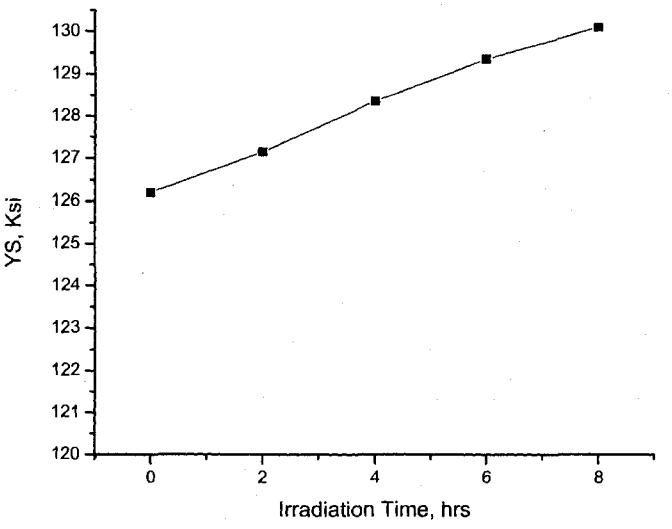

Figure 4-15 YS vs. Irradiation Time for Steel with 0.48 wt% Si

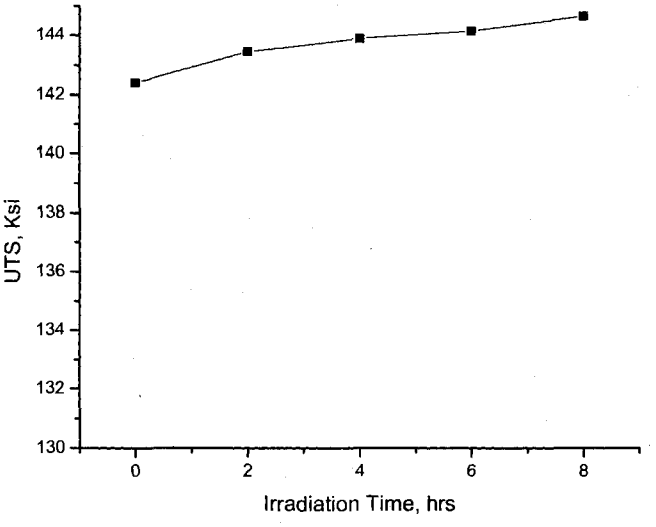

Figure 4-16 UTS vs. Irradiation Time for Steel with 0.48 wt% Si

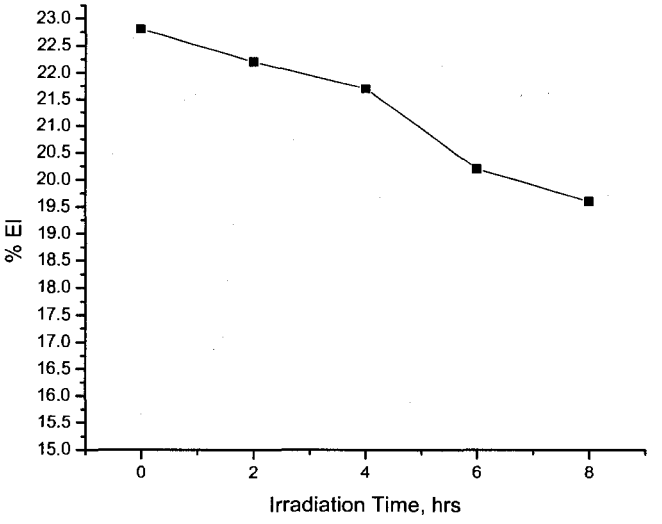

Figure 4-17 %El vs. Irradiation Time for Steel with 0.48 wt% Si

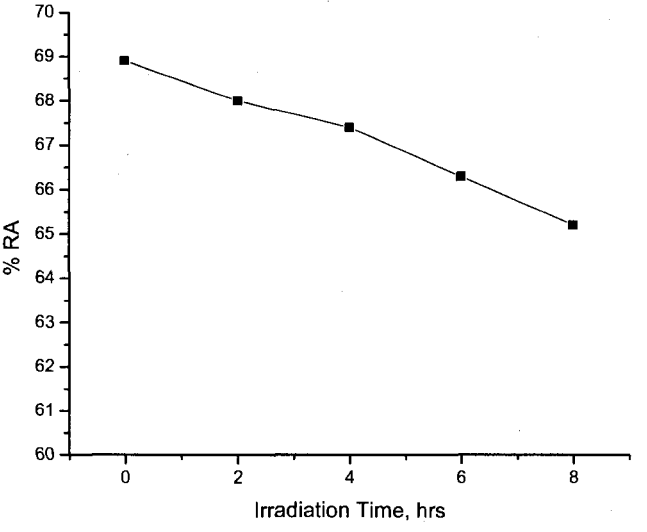

Figure 4-18 %RA vs. Irradiation Time for Steel with 0.48 wt% Si

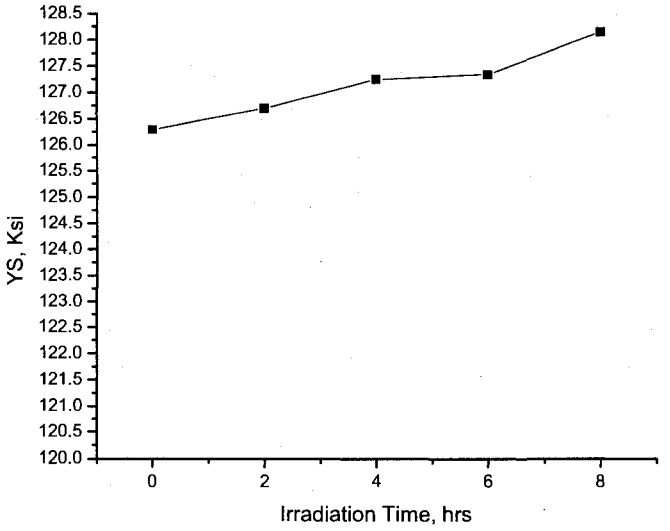

Figure 4-19 YS vs. Irradiation Time for Steel with 1.28 wt% Si

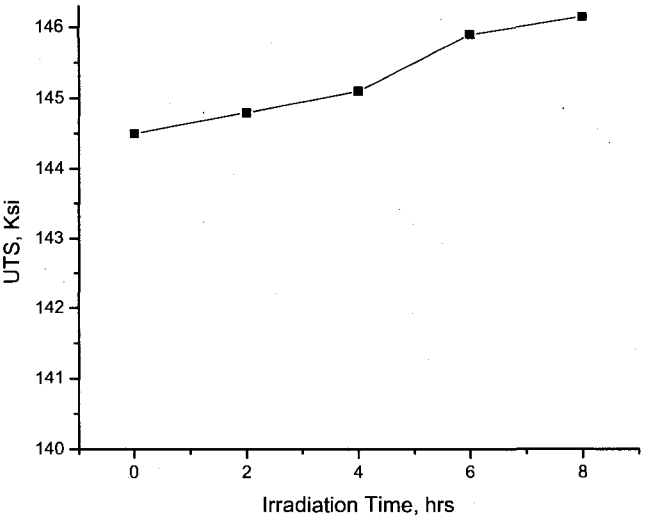

Figure 4-20 UTS vs. Irradiation Time for Steel with 1.28 wt% Si

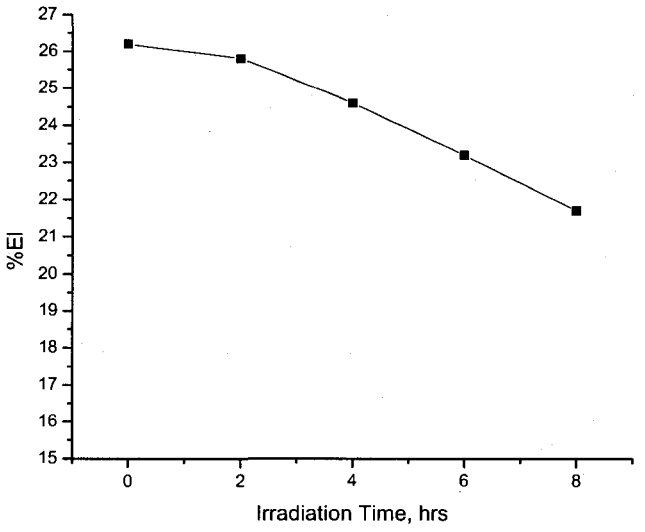

Figure 4-21 %El vs. Irradiation Time for Steel with 1.28 wt% Si

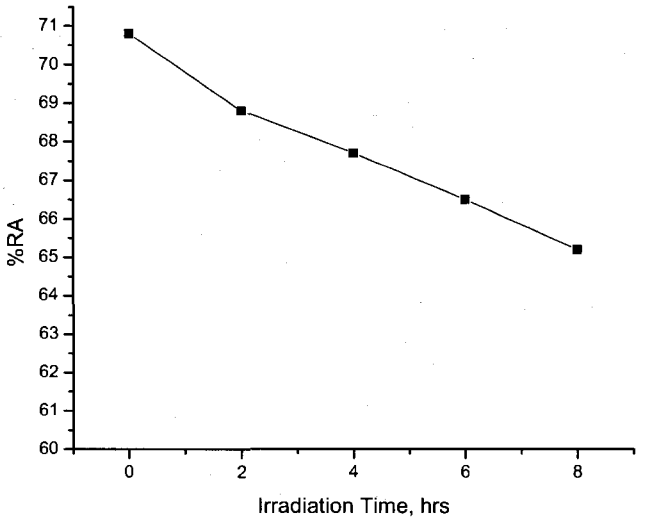

Figure 4-22 %RA vs. Irradiation Time for Steel with 1.28 wt% Si

4.4 Localized Corrosion Behavior

The susceptibility of P91 grade steel containing four levels of Si to localized corrosion (pitting and crevice corrosion) was determined in an acidic solution (pH ≈ 2.0-2.2) at 30 °C using the CPP technique based on electrochemical principles. The composition of the testing environment is given in Table 4-4. Prior to the CPP experiments, the potentiostat was calibrated, as discussed in Chapter 3. The resultant calibration curve is illustrated in Figure 4-23, which resembles the standard potentiodynamic polarization curve, shown in Figure 3-5.

Table 4-4 Chemical Composition of Test Solution (gm/liter)

Environment, pH	$CaCl_2$	K_2SO_4	$MgSO_4$	NaCl	$NaNO_3$	Na_2SO_4
Acidic, 2.0-2.2	2.77	7.58	4.95	39.97	31.53	56.74

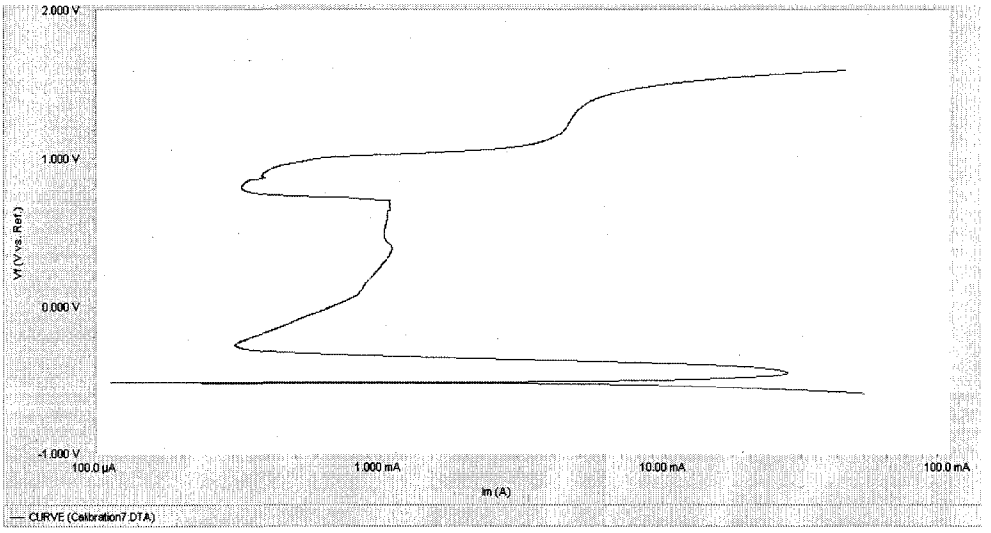

Figure 4-23 Generated Calibration Curve

The results of CPP testing indicate that all four heats of material exhibited an active to passive transition, showing both E_{corr} and E_{pit}. A CPP diagram of P91 grade steel containing 0.48 wt% Si is shown in Figure 4-24. The magnitudes of E_{corr} and E_{pit}, determined from the CPP diagrams, are given Table 4-5. These data indicate that E_{pit} gradually became more noble (positive) with increasing Si content, possibly due to the formation of more protective silicon oxide (SiO_2) layers on the metal surface. As to the effect of Si content on E_{corr}, its value gradually became nobler due to an increase in Si level from 0.48 to 1.28 wt%. However, at 1.77 wt% Si, E_{corr} became relatively more active (negative). The variations of E_{corr} and E_{pit} with Si content are illustrated in Figures 4-25 and 4-26, respectively. Interestingly, none of the polarized specimens did show any signs of pitting or crevice corrosion.

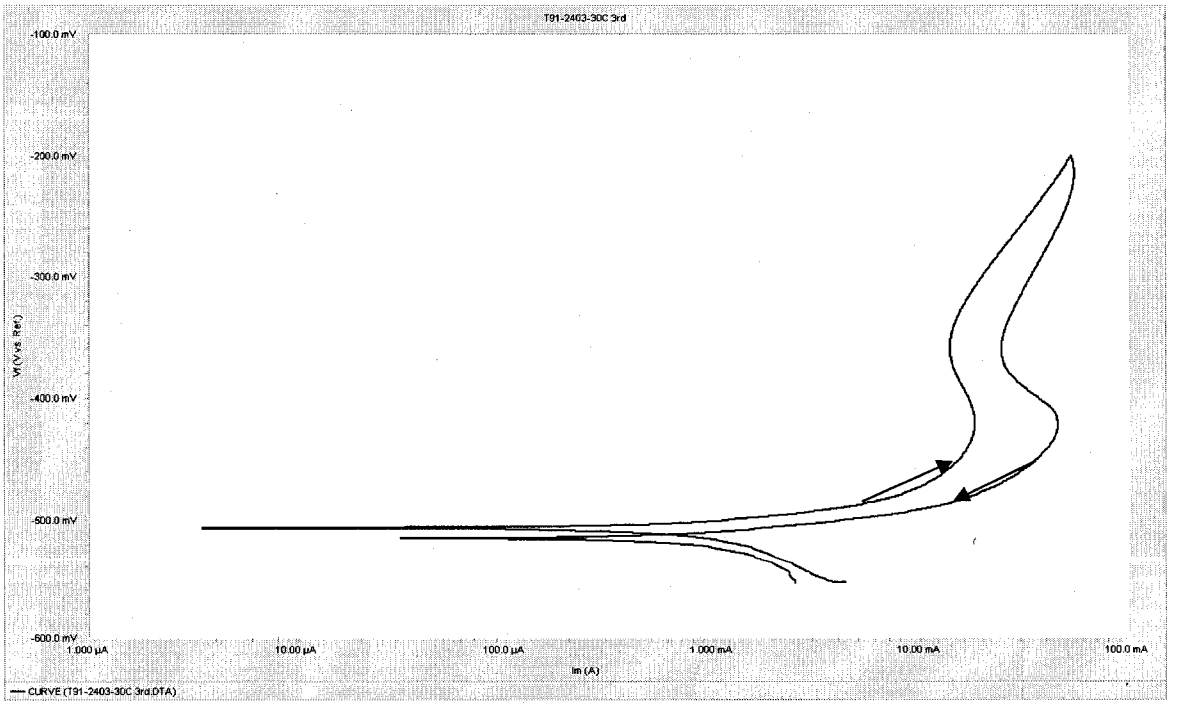

Figure 4-24 CPP Diagram of Steel with 0.96 wt% Si in 30 ^{0}C Acidic Solution

Table 4-5 Results of CPP Testing

Heat No./Si Content (wt%)	E_{corr}, mV (Ag/AgCl)	E_{pit}, mV (Ag/AgCl)
2525/0.48	-513	-430
2523/0.96	-506	-400
2526/1.28	-502	-380
2425/1.77	-516	-140

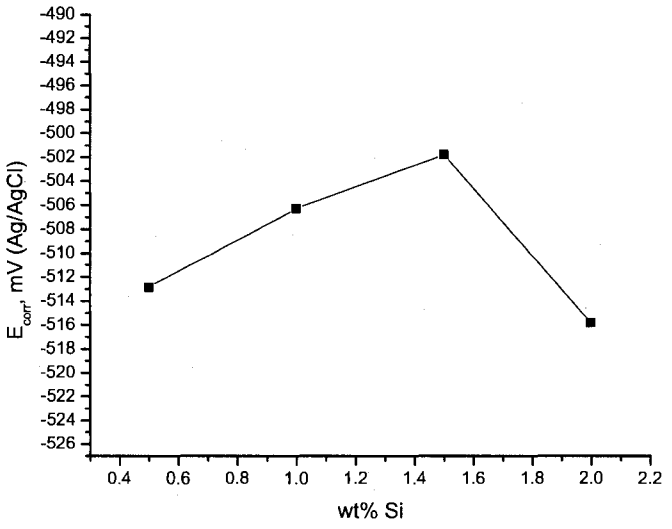

Figure 4-25 E_{corr} vs. Si Content

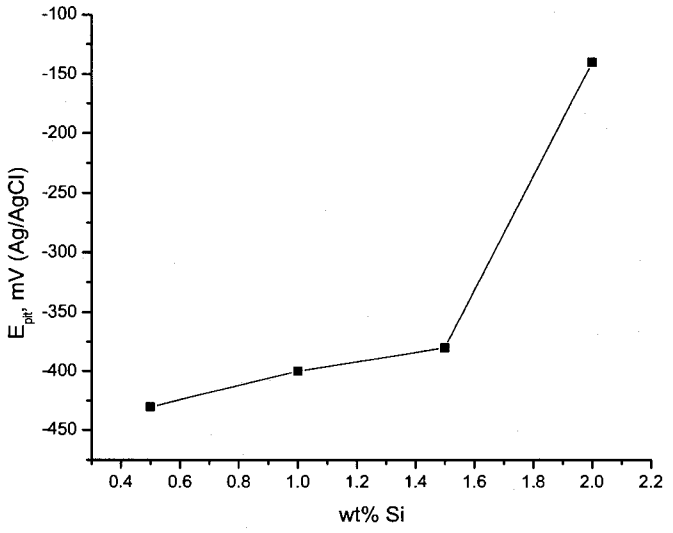

Figure 4- 26 E_{pit} vs.Si Content

4.5 Fractographic Evaluations

The SEM micrographs of tensile specimens of P91 grade steels containing 0.48, 0.96, 1.28 and 1.77 wt% Si, tested at ambient temperature and 550 °C, are illustrated in Figures 4-27 through 4-30, respectively. A comparative analysis of these micrographs revealed predominantly brittle failures at the primary fracture surfaces of all specimens tested at ambient temperature, which were characterized by the formation of cleavage facets and river marks, irrespective of the Si content. On the contrary, the specimens tested at 550 °C exhibited ductile failures, showing dimples and microvoids due to enhanced plasticity at the elevated temperature. It is interesting to note that the microvoids grew larger at 550 °C with increasing Si content.

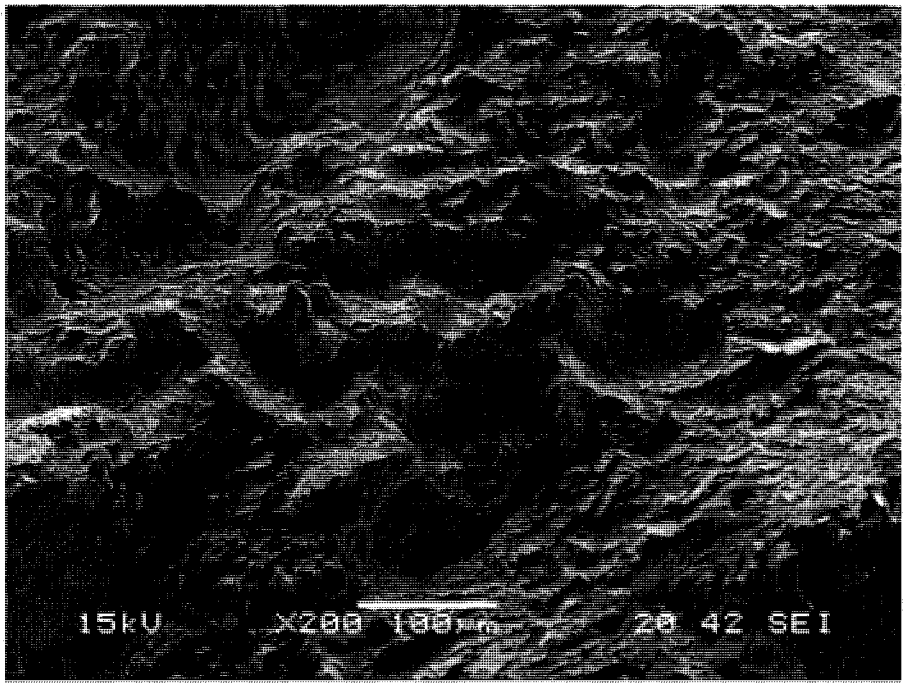

(a) Ambient Temperature

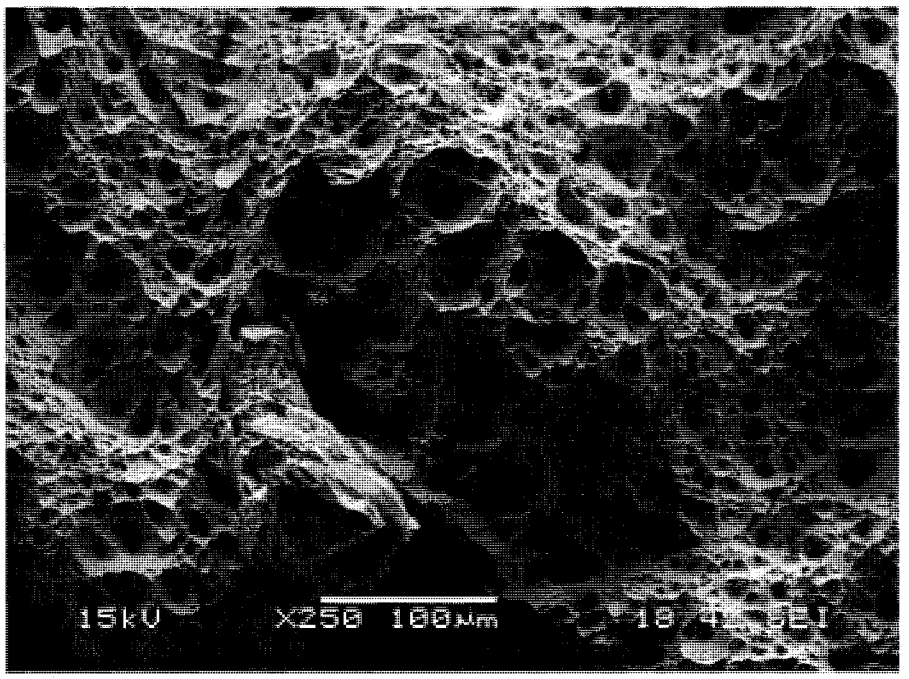

(b) 550 °C

Figure 4-27 SEM Micrograph of Steel Containing 0.48 wt % Si

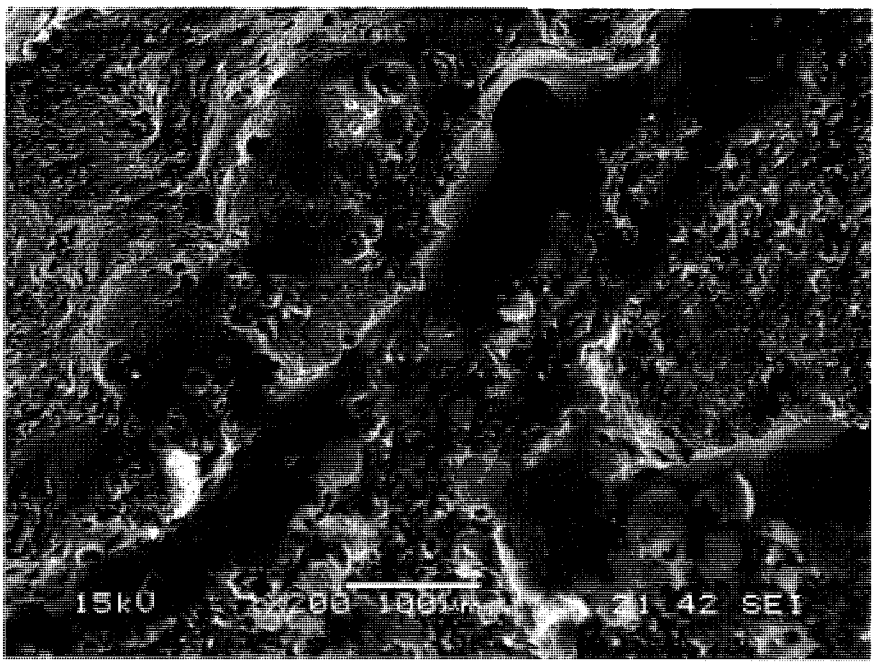

(a) Ambient Temperature

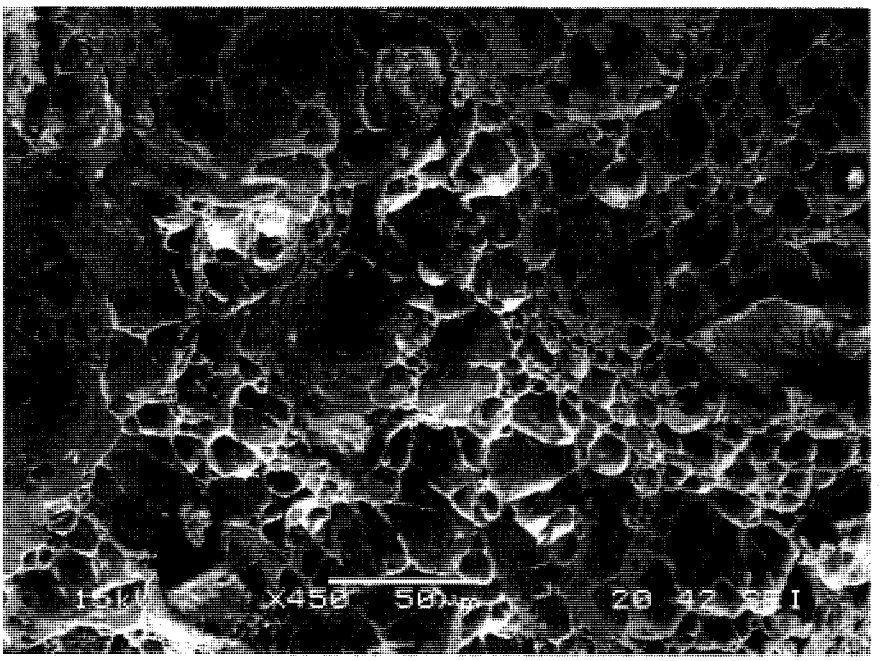

(b) 550 °C

Figure 4-28 SEM Micrograph of Steel Containing 0.96 wt % Si

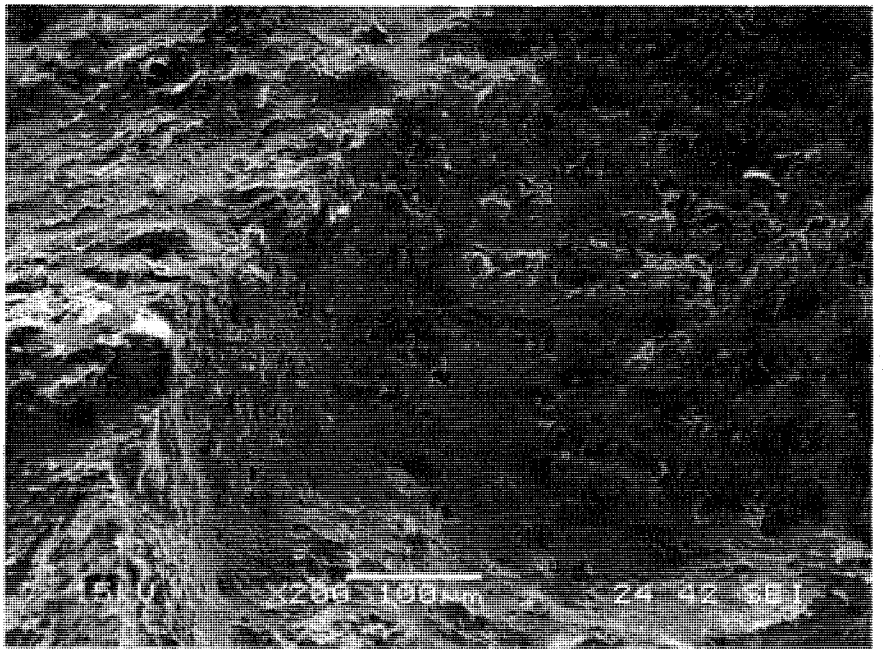

(a) Ambient Temperature

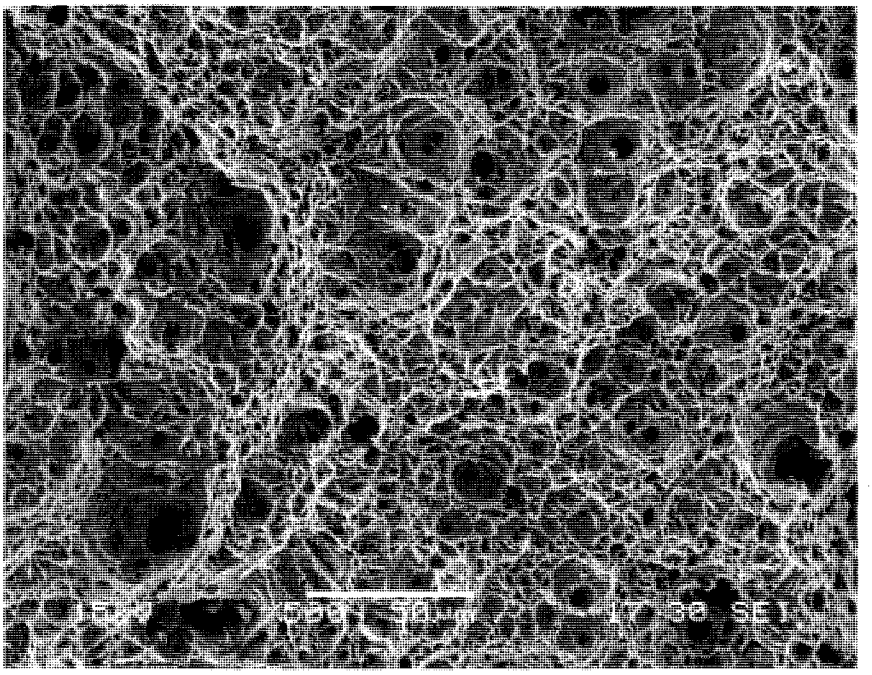

(b) 550 °C

Figure 4-29 SEM Micrograph of Steel Containing 1.28 wt % Si

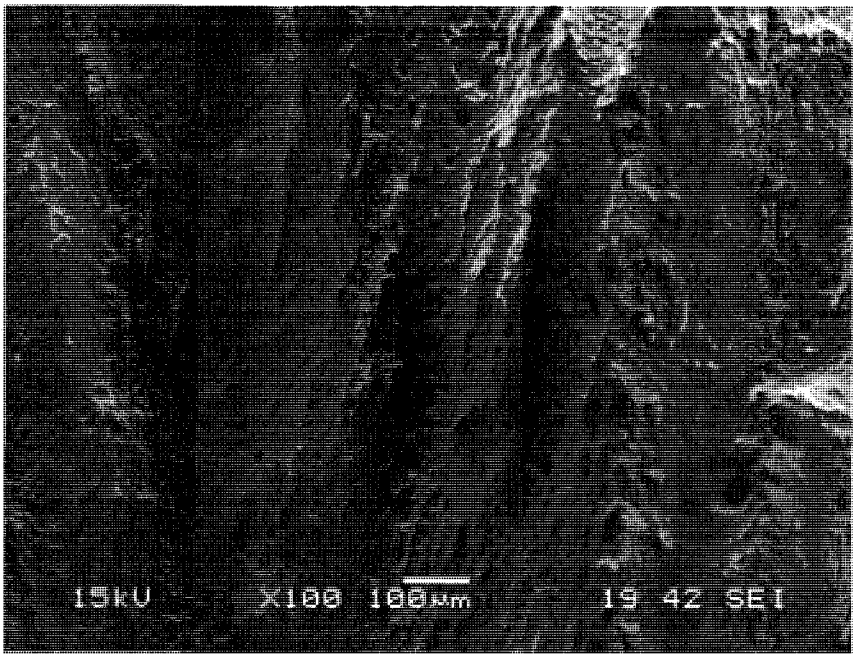

(a) Ambient Temperatur

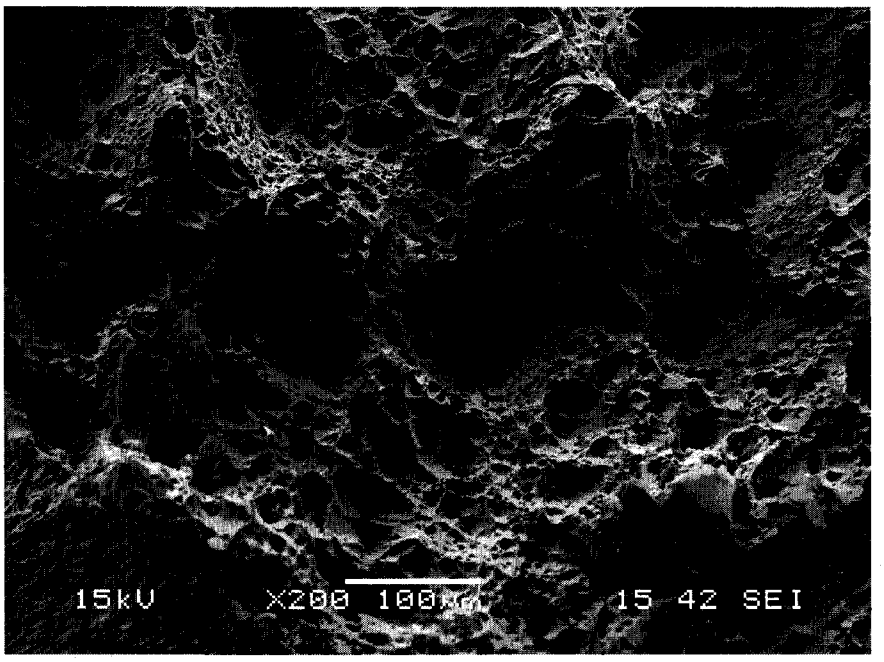

(b) 550 °C

Figure 4-30 SEM Micrograph of Steel Containing 1.77 wt % Si

The SEM micrographs at the primary fracture surfaces of the irradiated specimens tested under tensile loading at ambient temperature are illustrated in Figure 4-32. An examination of these micrographs clearly revealed severe brittle failures that were characterized by cleavage facets of appreciable depths. This type of fracture morphology is a common feature of brittleness of structural materials resulting from their exposure to irradiated environments. Thus, the resultant data justifiably demonstrate a detrimental effect of irradiation of P91 grade steels that eventually led to their enhancement of tensile strength and reduction in ductility, as discussed earlier in this chapter.

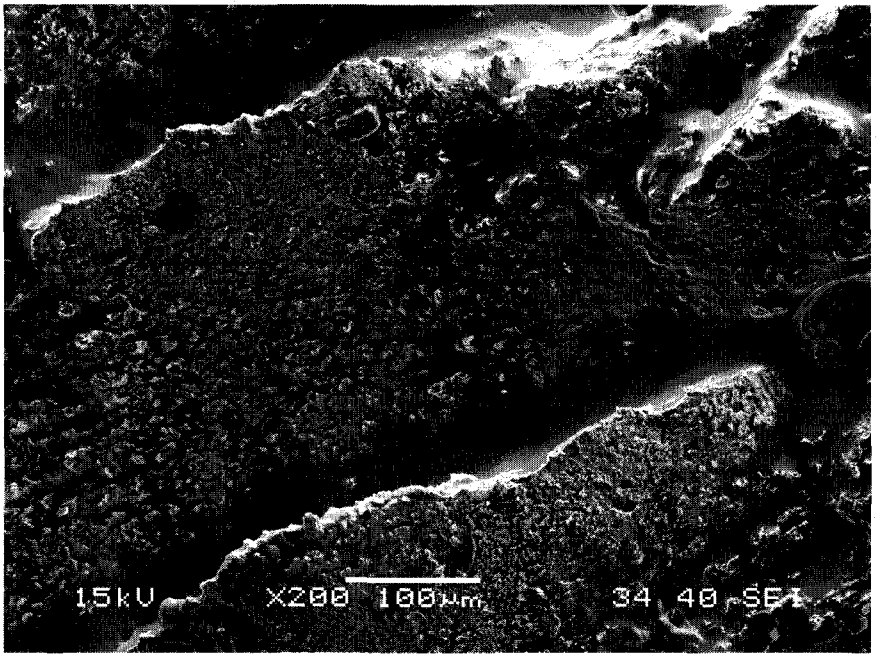

(a) Irradiation Time: 2 Hours

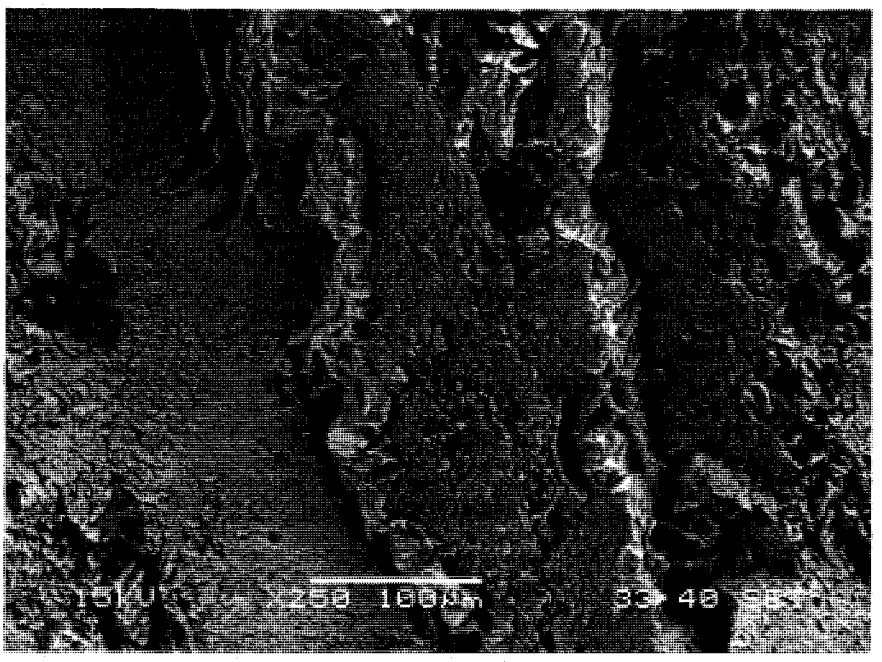

(b) Irradiation Time: 4 Hours

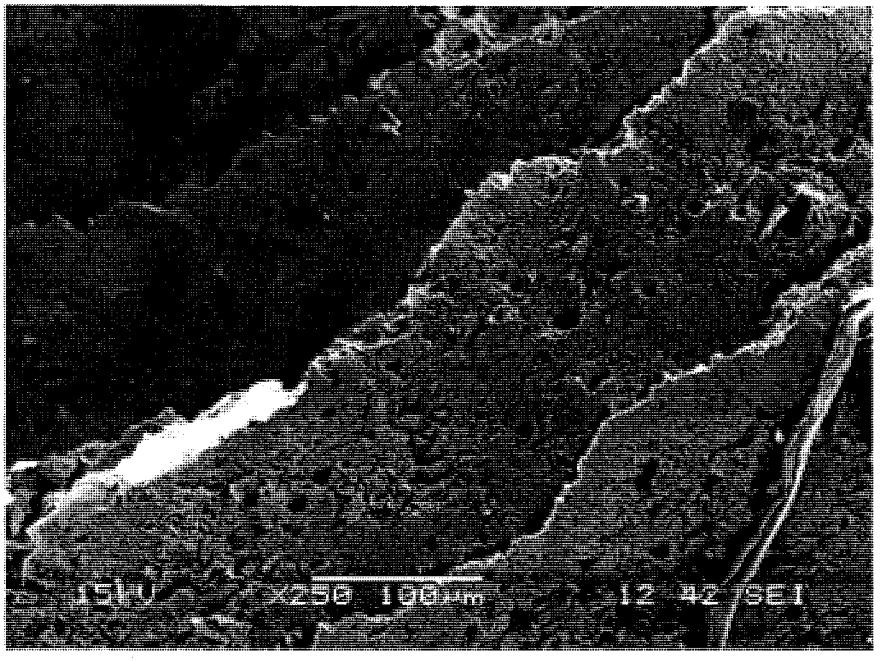

(c) Irradiation Time: 6 Hours

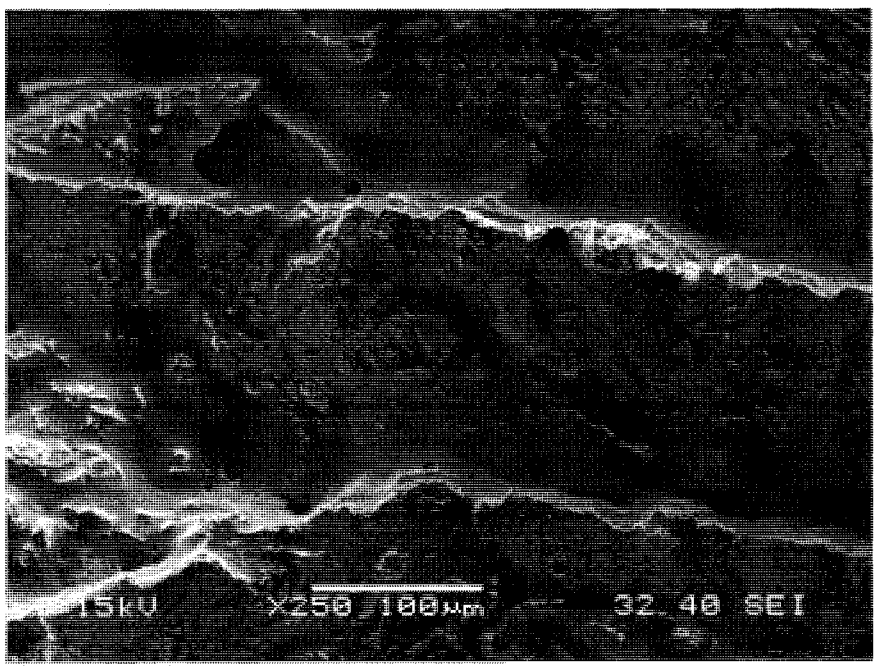

(d) Irradiation Time: 8 Hours

Figure 4-31 SEM Micrographs of Irradiated Steel Containing 1.28 wt% Si

CHAPTER 5

DISCUSSION

The role of silicon (Si) content on the tensile properties of modified 9Cr-1Mo steel, also known as P91 grade steel, has been explored in this investigation as a function of temperature. The effect of irradiation, on the mechanical behavior of this type of steel has also been studied at ambient temperature. Efforts have also been made to evaluate the localized corrosion susceptibility of these materials using an electrochemical method. Finally, the extent and morphology of failure of the tested tensile specimens have been determined by using SEM.

The results of tensile testing indicated that the magnitude of failure strain (e_f) was gradually reduced within a temperature regime of ambient to 300 °C, irrespective of the Si content. Additionally, serrations were seen in the engineering stress versus engineering strain (s-e) diagrams at temperatures up to 400 °C. Reduced e_f values and formation of serrations are associated with a metallurgical phenomenon, known as dynamic strain ageing that has previously been investigated by several researchers within the Materials Performance Laboratory at UNLV. Beyond this susceptible temperature range, the ductility of the tested materials in terms of %El and %RA was substantially increased due to enhanced plasticity. The temperature effect on ductility was most pronounced with steel containing 1.77 wt% Si.

P91 grade steel containing 0.48 and 1.28 wt% Si exhibited a susceptibility to radiation hardening due to irradiation by accelerator-induced electron beams, showing enhanced tensile strength but reduced ductility. As to the localized corrosion behavior, none of the tested materials exhibited any sign of pitting or crevice corrosion due to electrochemical polarization in an acidic solution at ambient temperature. The critical pitting potential (E_{pit}) gradually became more noble with increasing Si content, possibly due to the formation of more protective oxide films on the specimen surface.

Fractographic evaluations using SEM revealed brittle failures at the primary fracture surface of tensile specimens tested at ambient temperature. However, all specimens showed dimples and microvoids at 550 ^{o}C, indicating ductile failures due to enhanced plasticity. Finally, irrespective of the Si content, all irradiated specimens exhibited brittle (cleavage) failures suggesting the occurrence of radiation-hardening

CHAPTER 6

SUMMARY AND CONCLUSIONS

Martensitic P91 grade steels containing 0.48, 0.96, 1.28 and 1.77 wt% Si have been tested for evaluation of their tensile properties at temperatures relevant to the transmutation process. The effect of irradiation time using electron beams from LINAC on the ambient-temperature tensile properties has also been investigated. The localized corrosion behavior of these steels has been evaluated by the CPP technique. In addition, the morphologies of failure of the tested tensile specimens have been determined by SEM. The significant conclusions drawn from this work are summarized below.

- The metallurgical microstructures consisted of finely dispersed martensites within austenitic grains, and delta ferrites oriented in multiple directions.
- The s-e diagrams exhibited reduced e_f and serrations within some temperature regimes, suggesting the occurrence of the DSA phenomenon for which a mechanistic understanding is currently well established.
- The tensile specimens, subjected to the irradiation process, showed increased strength but reduced ductility with increasing irradiation time, indicating radiation-induced hardening of the P91 grade steels of varied Si content.
- E_{pit} became more noble with increasing Si content, suggesting a beneficial effect of thicker SiO_2 films in promoting the corrosion resistance of Fe-Cr-Mo steels.

- The SEM micrographs revealed brittle (cleavage) failures at the primary fracture surface of tensile specimens tested at ambient temperature. However, ductile failures characterized by dimples, were seen at 550 °C due to enhanced plasticity.
- All irradiated specimens showed severe brittle failures due to radiation hardening.

CHAPTER 7

SUGGESTIONS FOR FUTURE WORK

Performance of CPP experiments of P91 grade steels of varied Si content at elevated temperatures is suggested. Further, additional testing involving tensile specimens irradiated for longer durations could be useful.

APPENDIX A

TENSILE PROPERTIES EVALUATION WITHOUT ACTIVATION

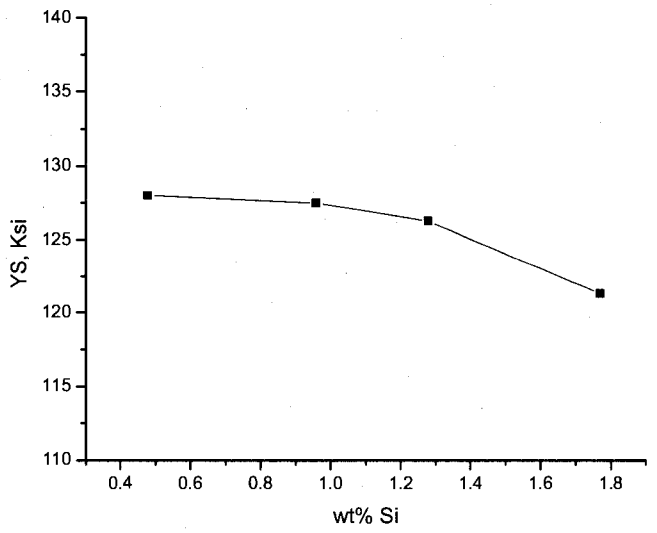

Figure 1 YS vs.wt% Si (RT)

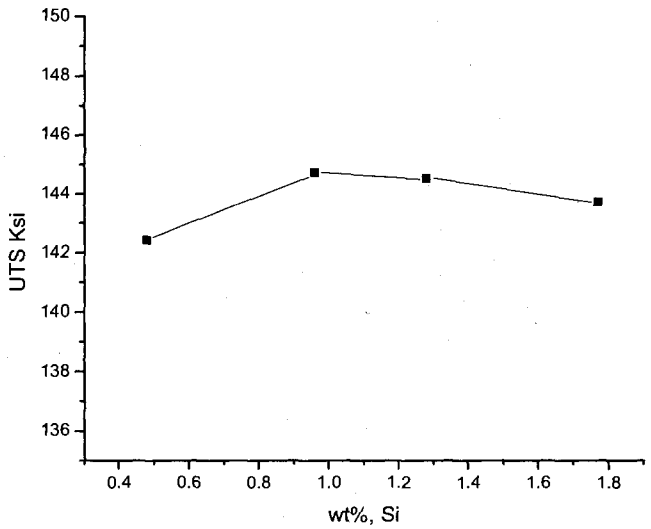

Figur2 UTS vs. wt% Si (RT)

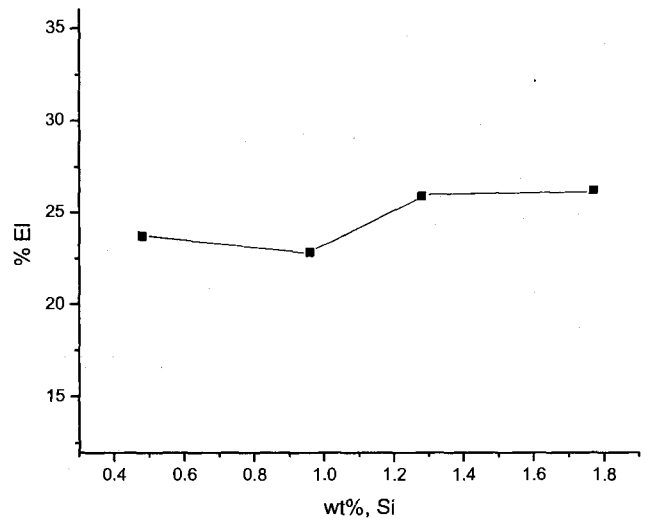

Figure 3 %El vs. wt% Si (RT)

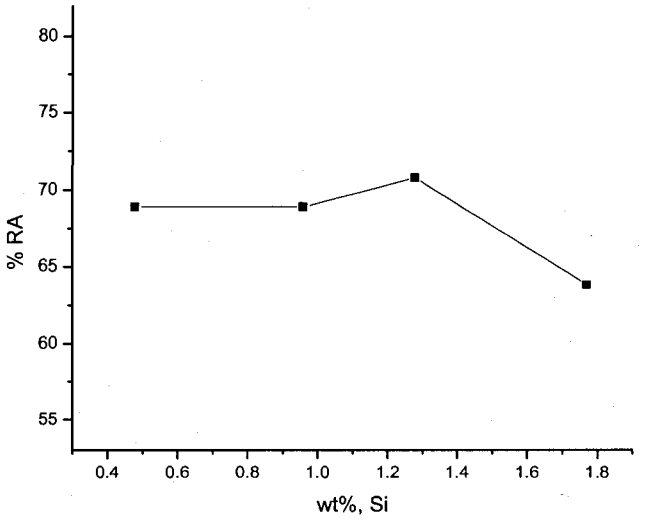

Figure-4 %RA vs. wt% Si (RT)

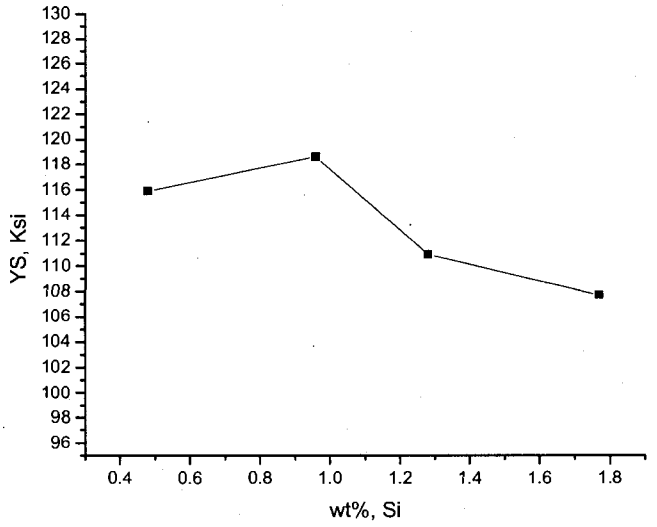

Figure -5 YS vs. wt% Si (150^0C)

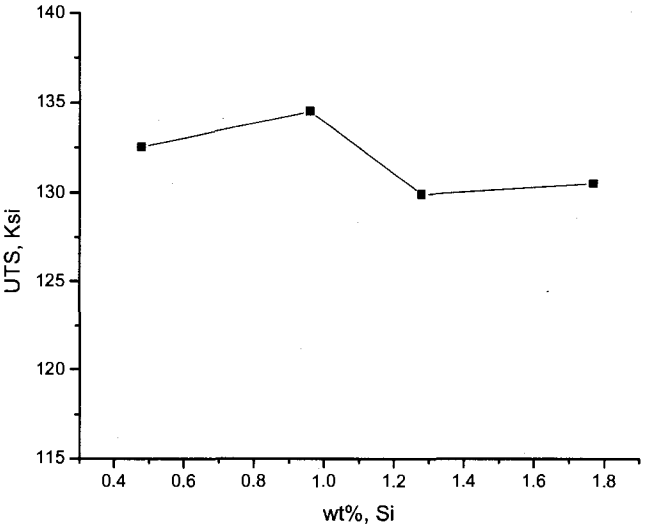

Figure -6 UTS vs. wt% Si (150^0C)

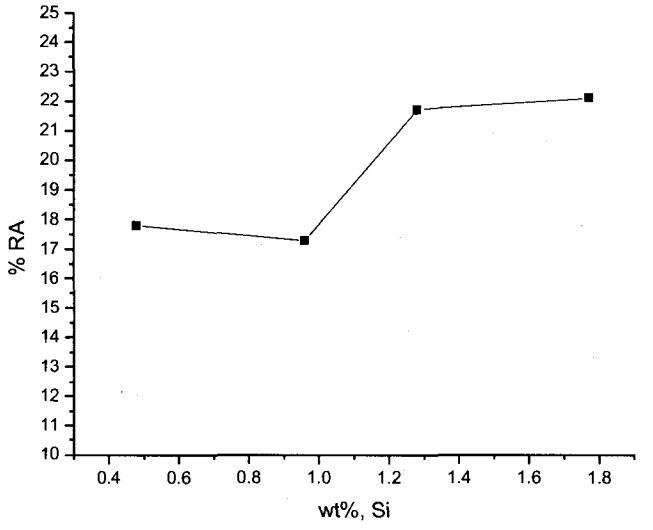

Figure-7 %RA vs. wt% Si (150^0C)

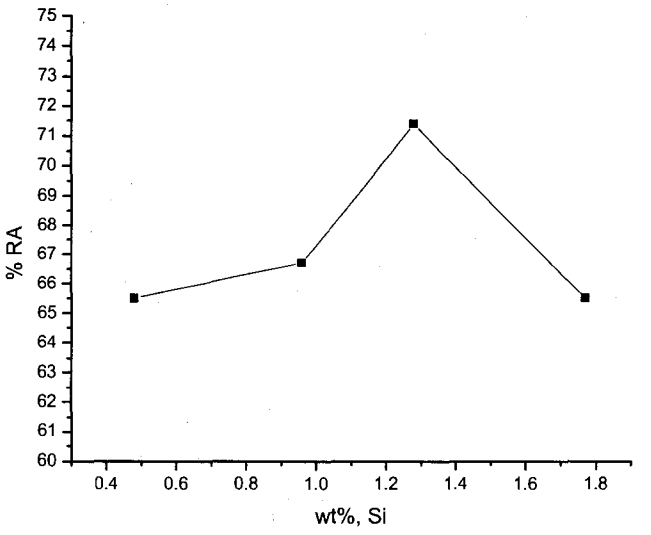

Figure-8 %RA vs. wt% Si (150^0C)

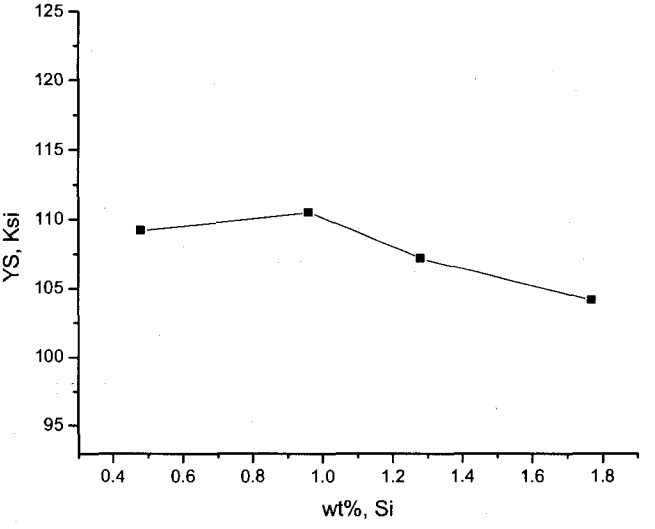

Figure-9 YS vs. wt% Si (300^0C)

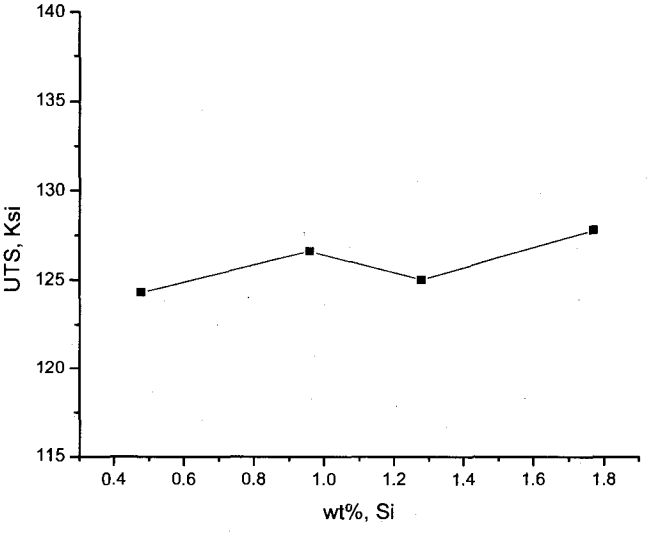

Figure -10 UTS vs. wt% Si (300^0C)

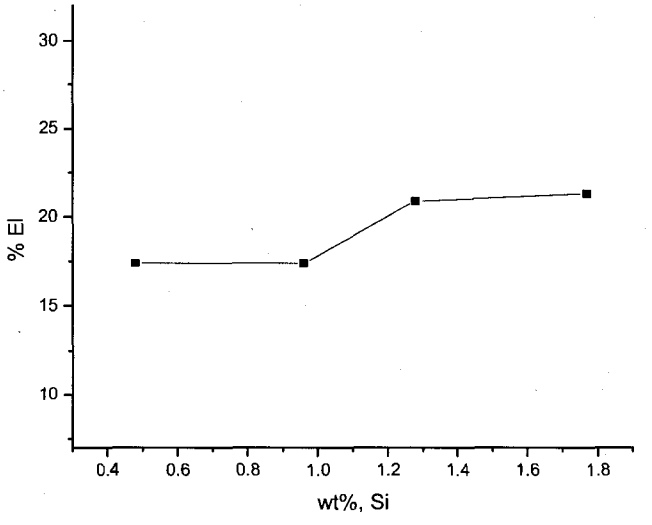

Figure -11 %El vs. wt% Si (300^0C)

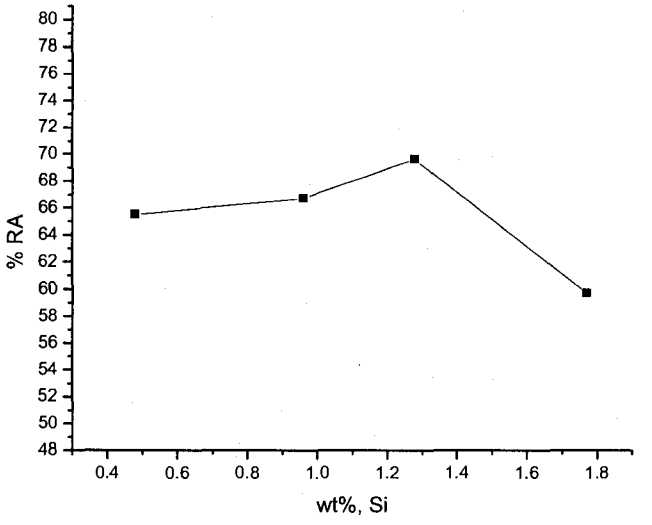

Figure-12 %RA vs. wt% Si(300^0C)

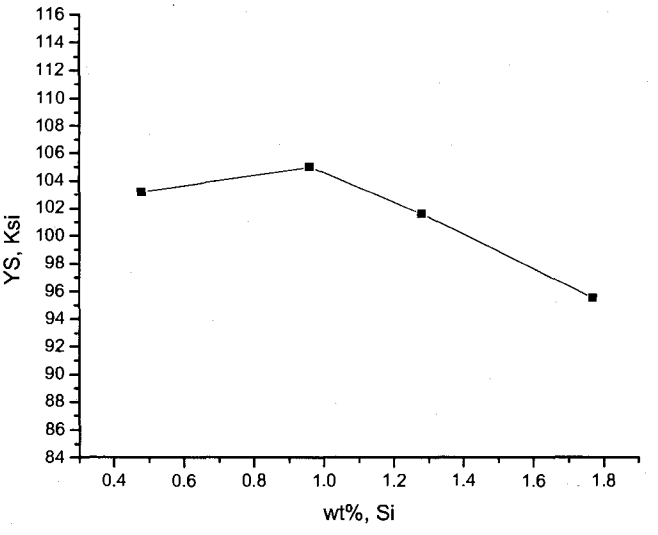

Figure-13 YS vs. wt% Si (400^0C)

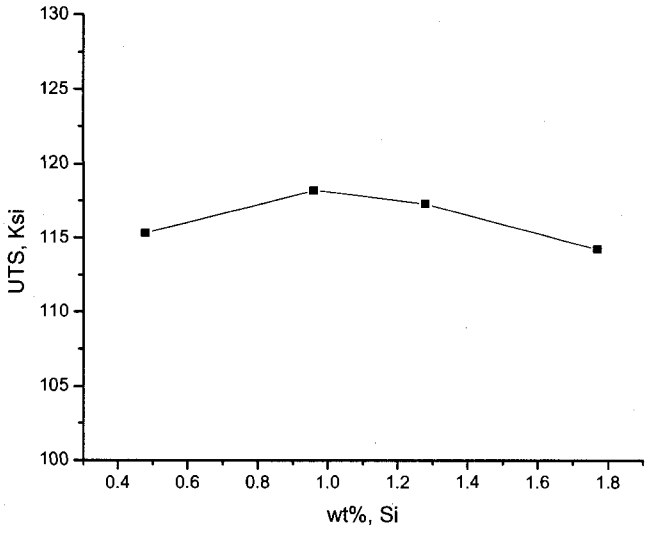

Figure-14 UTS vs. wt% Si (400^0C)

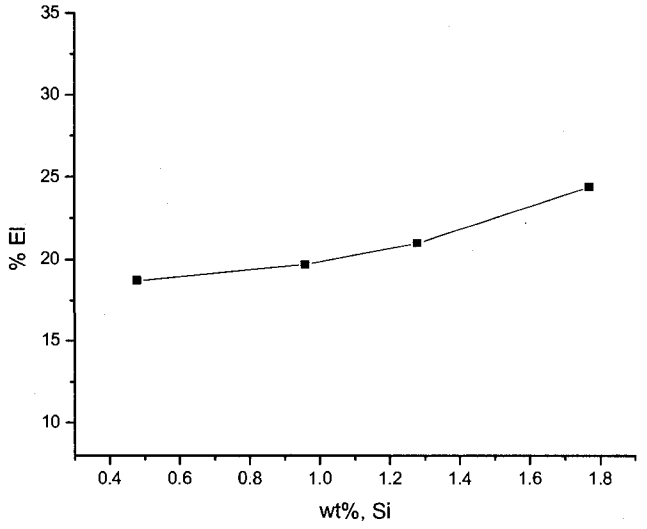

Figure-15 %El vs. wt% Si (400^0C)

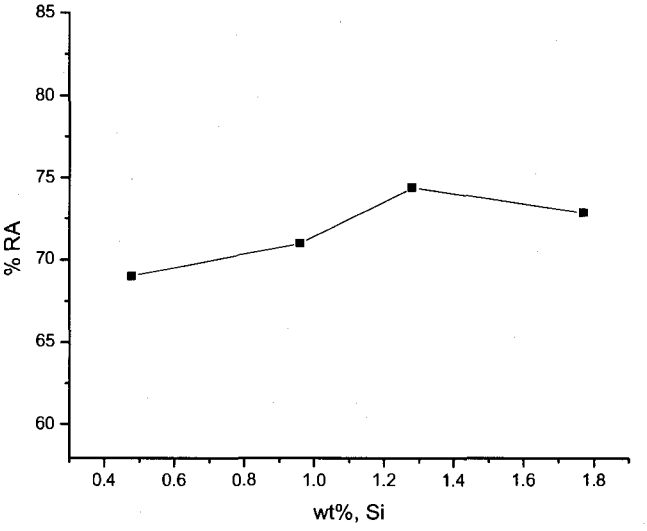

Figure-16 %RA vs. wt% Si (400^{0}C)

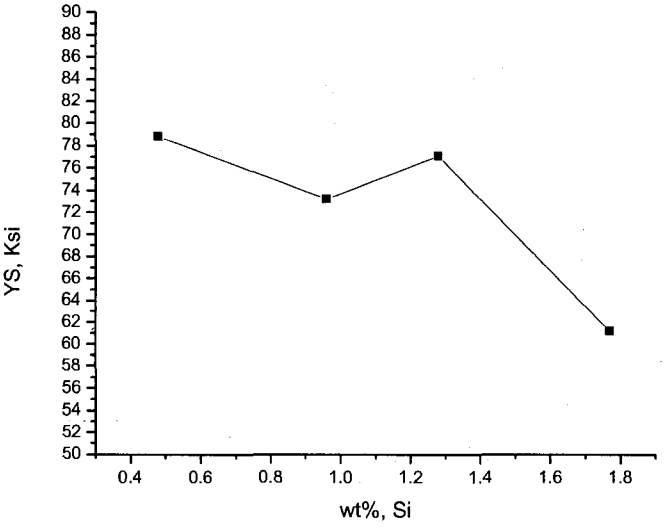

Figure-17 YS vs. wt% Si (550^{0}C)

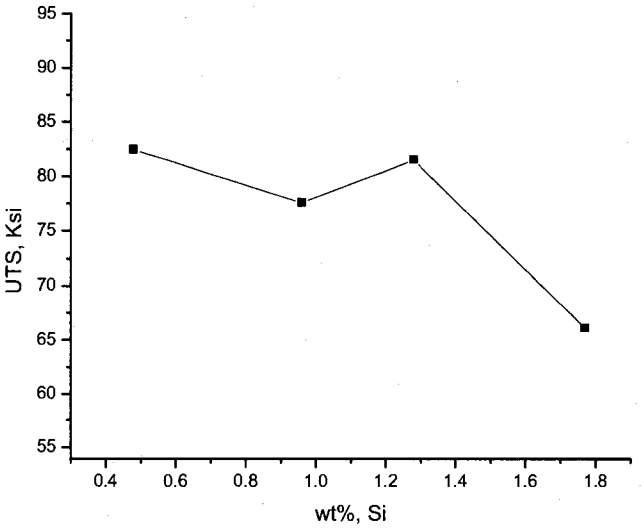

Figure-18 UTS vs. wt% Si (550^0C)

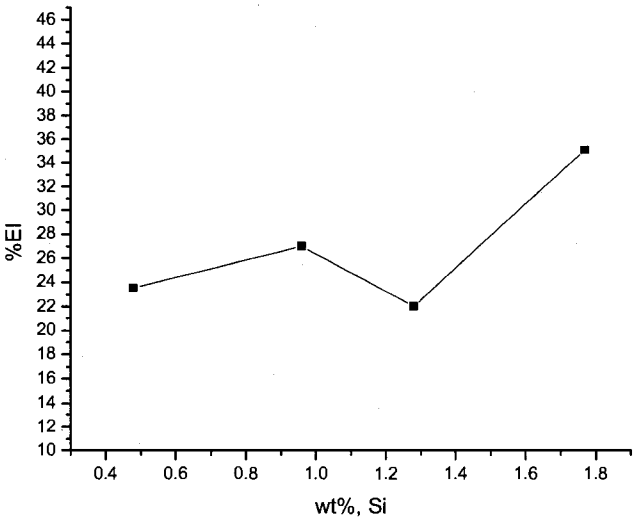

Figure-19 %El vs. wt% Si (550^0C)

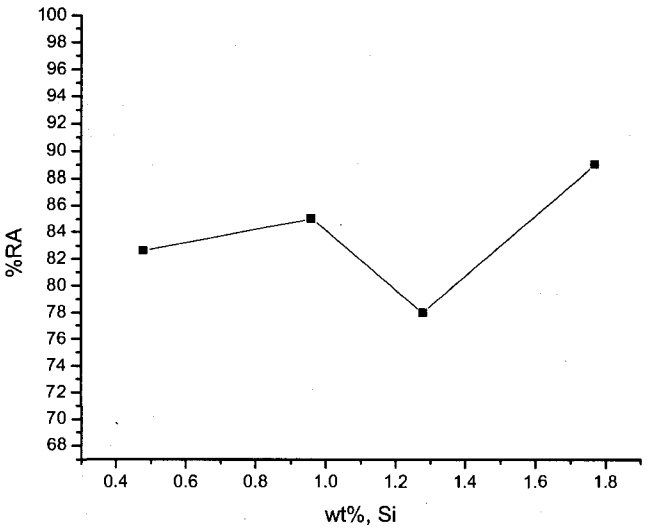

Figure-20 %RA vs. wt% Si (550^0C)

APPENDIX B

FRACTOGRAPHY

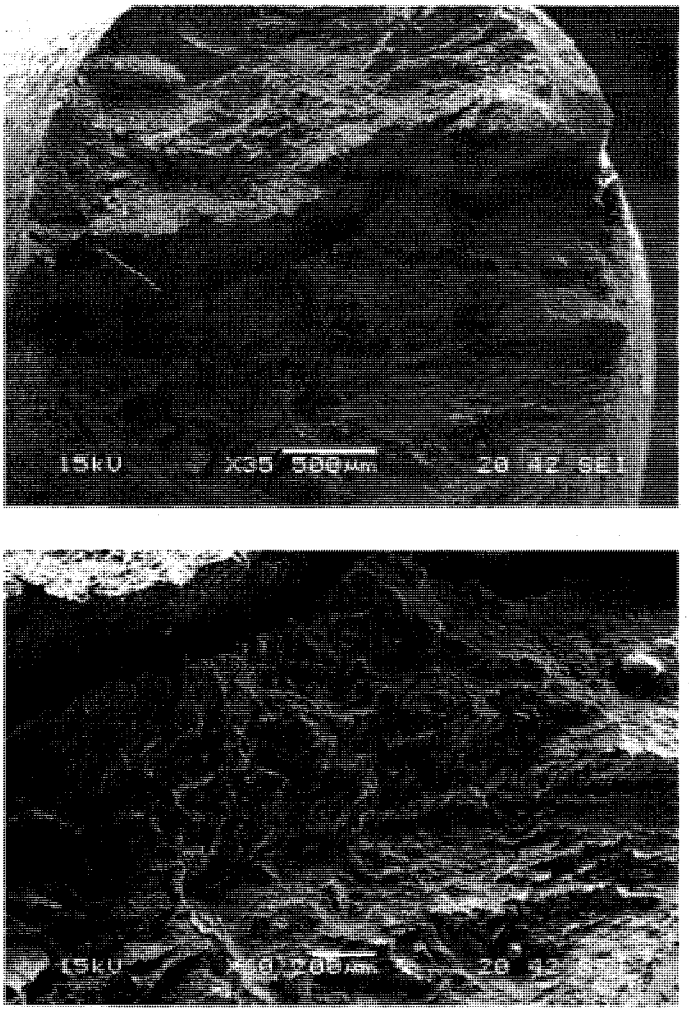

Figure 1 SEM Micrographs of steel containing .48 wt % Si at RT

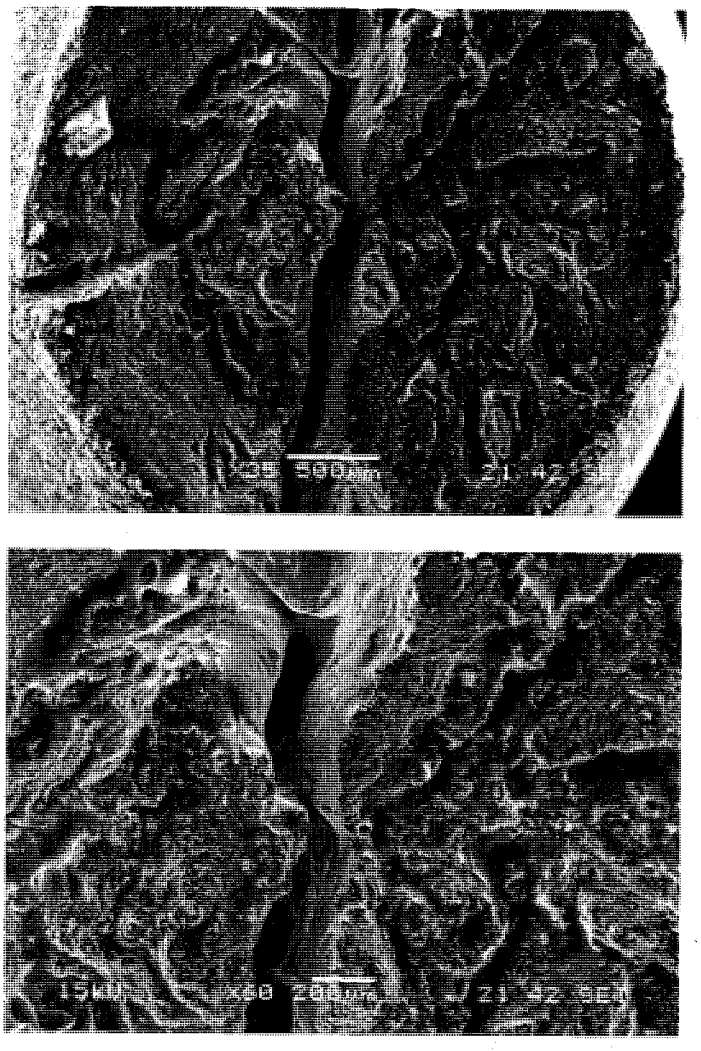

Figure 2 SEM Micrographs of steel containing .96 wt % Si at RT

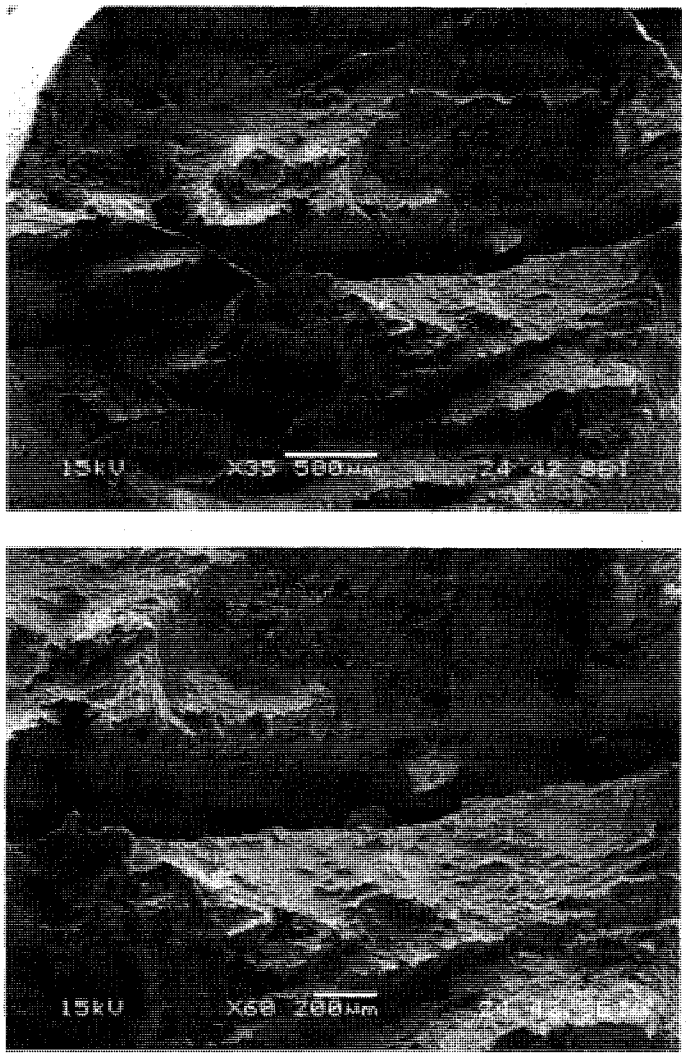

Figure 3 SEM Micrographs of steel containing 1.28 wt % Si at RT

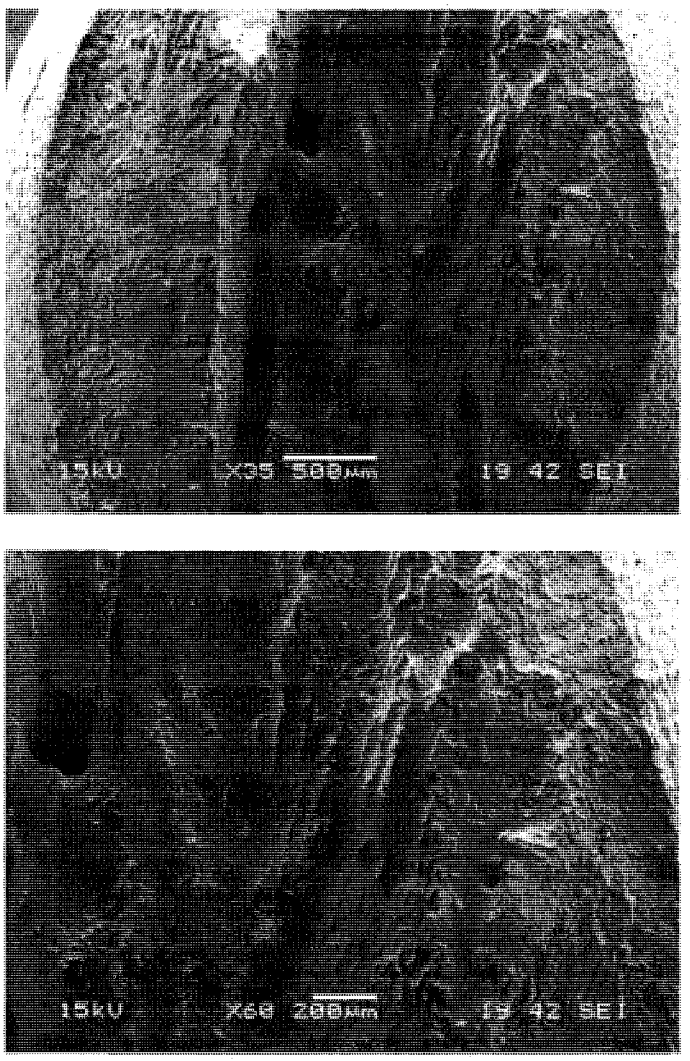

Figure 4 SEM Micrographs of steel containing 1.77 wt % Si at RT

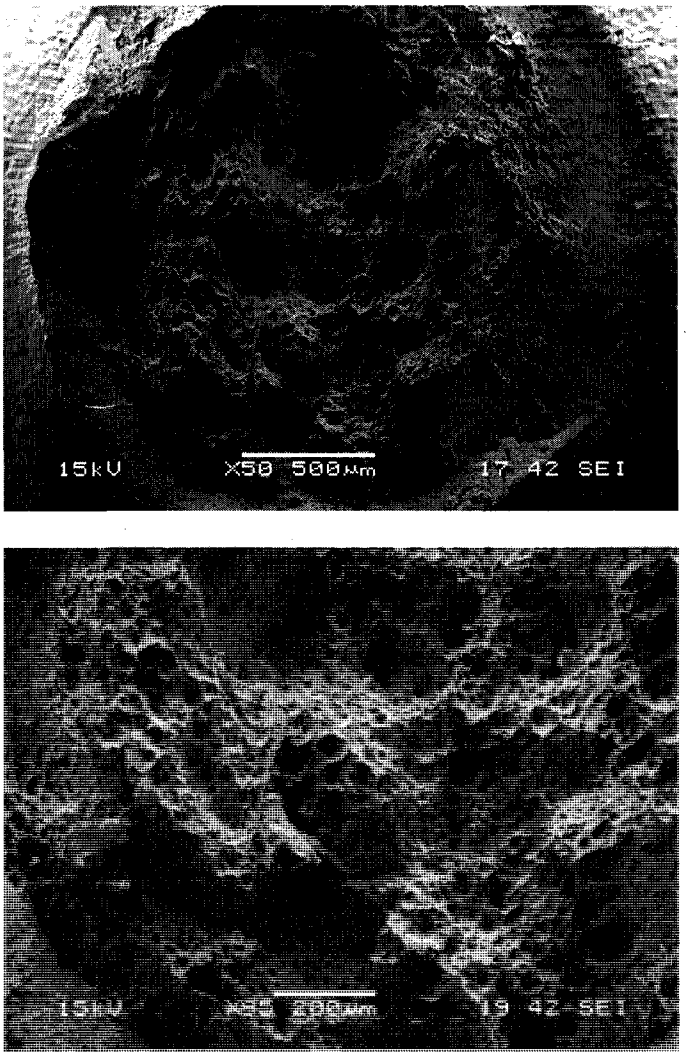

Figure-5 SEM Micrographs of steel containing .48 wt % Si at 550^0C

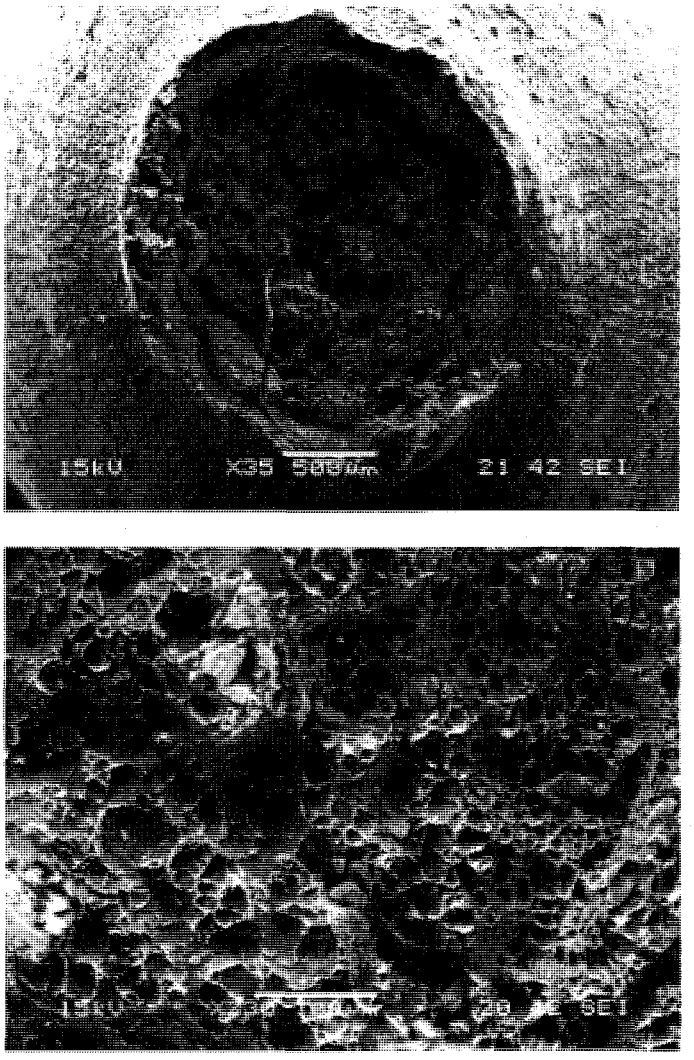

Figure-6 SEM Micrographs of steel containing .96 wt % Si at 550^0C

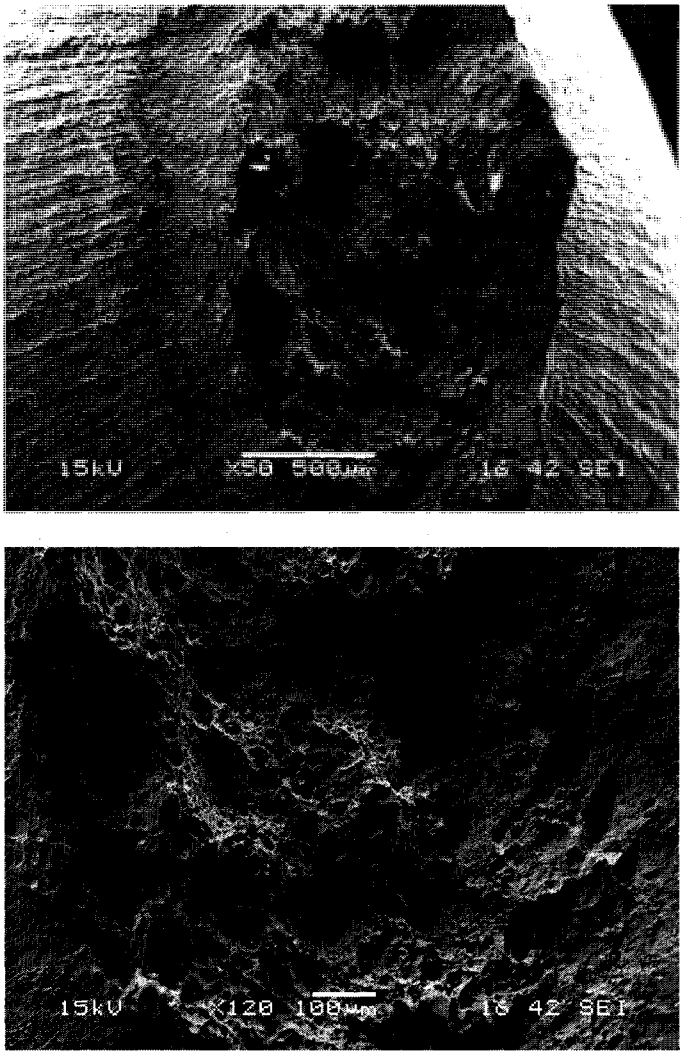

Figure-7 SEM Micrographs of steel containing 1.77 wt % Si at 550^0C

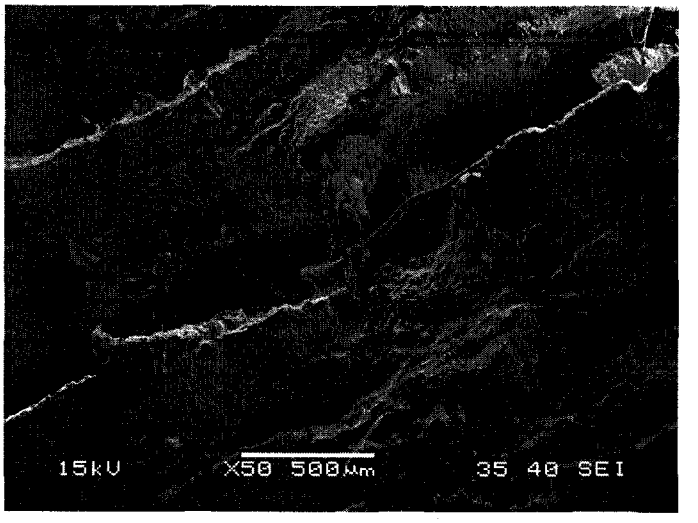

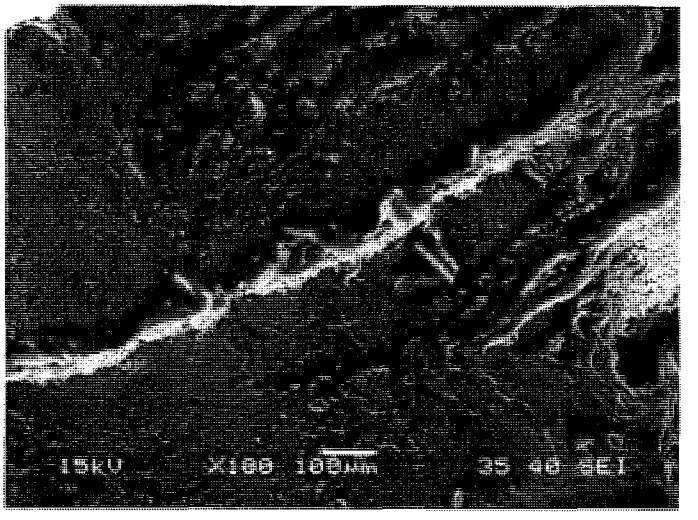

(a) Two hours of Activation

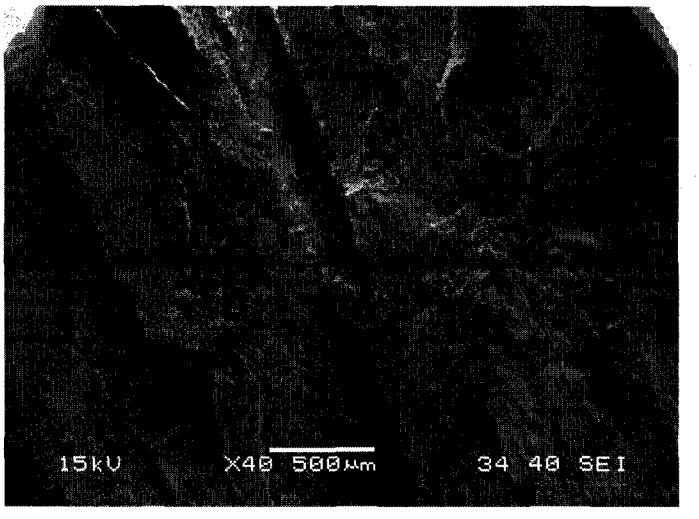

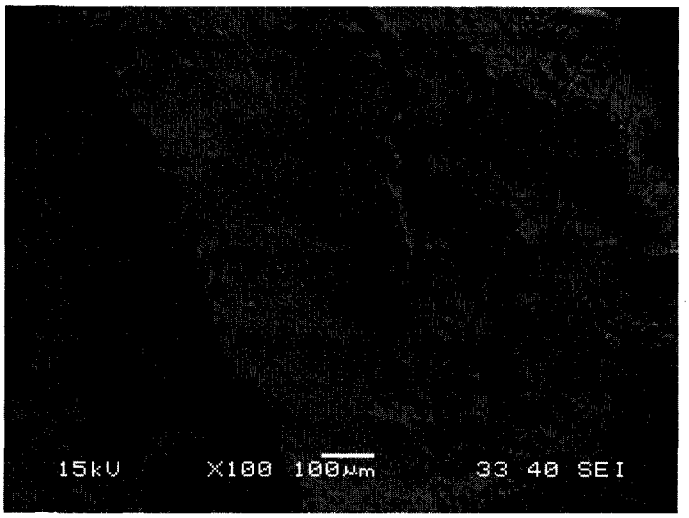

(b) Four hours of Activation

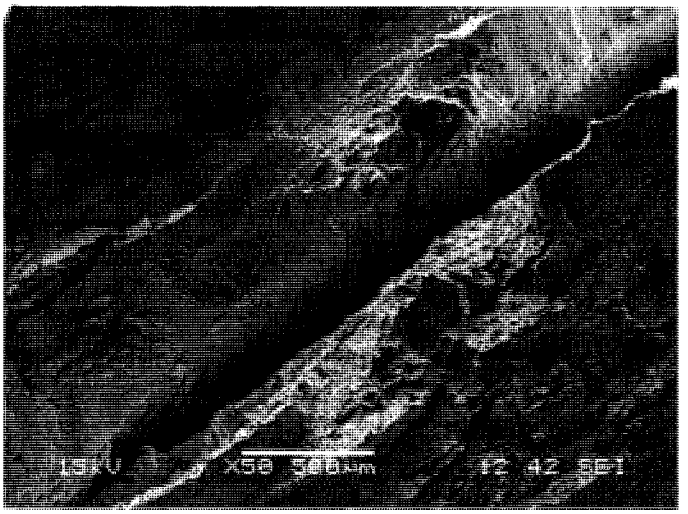

(C) Six hours of Activation

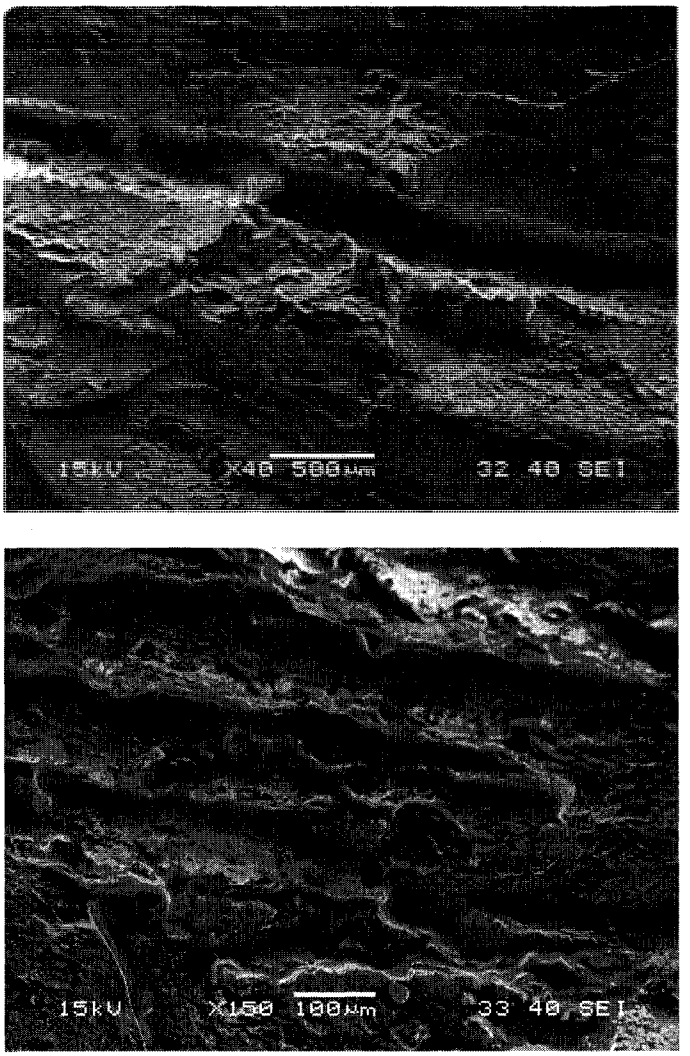

(D)Eight hours of Activation

Figure 8 SEM Micrographs of Fracture Surface of Activated Specimens with 1.28 wt% Si

APPENDIX C

UNCERTAINTY ANALYSES OF EXPERIMENTAL RESULTS

The parameters like lengths, times etc. are directly measured in any experiment. The instruments used to determine these measurements may vary in quality every time they are being used. Also, the parameters that are out of control of the researcher might cause undesired variations in these measurements. Efforts were taken to repeat all the experiments in order to determine an average value. However, the undesired variations might have caused variations in the derived results. These variations if caused by the machines used in the experiments can be reduced by calibrating them on a timely basis. However the variations caused due to human errors and environmental factors cannot be avoided. Uncertainty analysis of these derived results determines the variations/errors in them.

A precise method of estimating uncertainty in experimental results has been presented by Kline and McClintock. The method is based on a careful specification of the uncertainties in the various primary experimental measurements. When the plus or minus notation is used to designate the uncertainty, the person making this designation is stating the degree of accuracy with which he or she believes the measurement has been made. It is notable that this specification is in itself uncertain because the experiment is naturally

uncertain about the accuracy of these measurements. If a very careful calibration of an instrument has been performed recently, with standards of very high precision, then the experimentalist will be justified in assigning a much lower uncertainty to measurements than if they were performed with a gage or instrument of unknown calibration history.

Most of the instruments in the Materials Performance Laboratory (MPL) were calibrated on a regular basis by Bechtel Nevada using standards with very high precision. Thus, it is expected that the resultant data presented in this thesis would have very insignificant uncertainty. The uncertainties in the results of this investigation are calculated by using the Kline and McClintock Method. The equation used for this method is given below.

$$W_R = \left[\left(\frac{\partial R}{\partial x_1} w_1 \right)^2 + \left(\frac{\partial R}{\partial x_2} w_2 \right)^2 + \cdots + \left(\frac{\partial R}{\partial x_n} w_n \right)^2 \right]^{\frac{1}{2}} \qquad \text{Equation A1}$$

Where, W_R = the uncertainty in the results

R = the given function of the independent variables $x_1, x_2, \ldots\ldots x_n$)

$R = R(x_1, x_2, \ldots\ldots x_n)$

$w_1, w_2, \ldots\ldots w_n$ = the uncertainty in the independent variables

D.1 Uncertainty Calculation in Instron Results

The results generated from the Instron testing equipment are stress (σ), percentage elongation (%El), and percentage reduction in area (%RA). The stress is based on the load (P) and the initial cross-sectional area (A_i) of the tested specimen. The

%El is based on the change in length (Δl) during the testing and the %RA is based on the initial and final cross-sectional areas (A_i and A_f). The magnitude of P was obtained from the load-cell of the Instron unit. The values for Δl, A_i, and A_f were calculated based on measurements by a caliper. The uncertainties in load-cell and caliper were ± 0.03% lbs and ± 0.001 inch, respectively, obtained from the calibration. The uncertainty in the initial notched diameter was ± 0.001, which was provided by the manufacturer and the uncertainty in the final notched diameter was ± 0.001 obtained by using the caliper.

$$\sigma = P/A_i \qquad \text{Equation A2}$$

D.1.1 Calculation of Uncertainty in Stress (U_σ)

$U_\sigma = U_{(P, Ai)}$

$U_{Ai} = (U_{Di})^2$

Uncertainty in load-cell = ± 0.03% lb

Uncertainty in caliper = ± 0.001 inch.

Sample calculation:

For yield stress (YS) = 129 ksi

The measured load (P) = 6321 lbf

Uncertainty in load (U_P) = 6321 × 0.0003

= ± 1.8963

Uncertainty in cross-sectional area (U_{Ai}) for the smooth tensile specimen:

Initial Diameter (D_i) = 0.2505 inch.

Uncertainty in diameter (U_{Di}) = ± 0.001 inch.

$$\text{Area } (A_i) = \frac{\pi D_i^{\,2}}{4}$$

$$= 0.0493 \text{ inch}^2$$

$$\frac{dA_i}{dD_i} = \frac{\pi D_i}{2}$$

$$= 0.393$$

$$\text{Uncertainty in area, } U_{Ai} = \left[\left(\frac{dA_i}{dD_i} \cdot U_{Di}\right)^2\right]^{\frac{1}{2}}$$

$$= 0.393 \times 0.001$$

$$= \pm 0.000393$$

$$\text{Uncertainty in stress, } U_\sigma = \left[\left(\frac{\partial \sigma}{\partial P} \cdot U_P\right)^2 + \left(\frac{\partial \sigma}{\partial A_i} \cdot U_{A_i}\right)^2\right]^{\frac{1}{2}} \qquad \text{Equation A3}$$

$$\sigma = \frac{P}{A_i}$$

$$\frac{\partial \sigma}{\partial P} = \frac{1}{A_i}$$

$$= 20.284$$

$$\frac{\partial \sigma}{\partial A_i} = -\frac{P}{A_i^{\,2}}$$

$$= -2600716.3866$$

Now providing all the numerical values in Equation A3 obtained from the calculation, it is found that,

$$U_\sigma = \left[(20.284 * 1.8963)^2 + (2600716.3866 * 0.000393)^2\right]^{\frac{1}{2}}$$

$$= 1022.81 \text{ psi} = \pm 1.023 \text{ ksi}$$

One example of the use of the uncertainty analysis is shown in this section. This can be implemented to all experimental results discussed in this dissertation.

D.1.2 Calculation of Uncertainty in Percentage Elongation ($U_{\%El}$)

Sample calculation:

Change in length (Δl) = 0.233 inch.

Gage length (l) = 1 inch.

$$\%El = \frac{\Delta l}{l} \cdot 100$$

Uncertainty in Δl ($U_{\Delta l}$) = $\pm$ 0.001

Uncertainty in %El ($U_{\%El}$),

$$U_{\%El} = \left[\left(\frac{d\%El}{d\Delta l} \cdot U_{\Delta l} \right)^2 \right]^{\frac{1}{2}} \qquad \text{Equation A4}$$

$$\frac{d\%El}{d\Delta l} = \frac{100}{l}$$

$$= 100$$

Providing all the calculated values in Equation A4, it is found that,

$$U_{\%El} = \left[(100 * 0.001)^2 \right]^{\frac{1}{2}}$$

$$U_{\%El} = \pm 0.1$$

One example of the use of the uncertainty analysis is shown in this section. This can be implemented to all experimental results discussed in this dissertation.

D.1.3 Calculation of Uncertainty in Percentage Reduction in Area ($U_{\%RA}$)

Sample calculation:

For %RA = 60.0%

Uncertainty in initial cross-sectional area (U_{Ai}) for the smooth specimen:

Initial Diameter (D_i) = 0.2505 inch.

Uncertainty in initial diameter,

$(U_{Di}) = \pm 0.001$ in

$$\text{Area } (A_i) = \frac{\pi D_i^2}{4}$$

$$= 0.0493 \text{ inch}^2$$

$$\frac{dA_i}{dD_i} = \frac{\pi D_i}{2}$$

$$= 0.393$$

Uncertainty in initial cross-sectional area,

$$U_{A_i} = \left[\left(\frac{dA_i}{dD_i} \cdot U_{D_i} \right)^2 \right]^{\frac{1}{2}}$$

$$= 0.393 \times 0.001$$

$$= \pm 0.000393$$

Uncertainty in final cross-sectional area (U_{Af}) for the smooth specimen:

Final Diameter (D_f) = 0.1584 inch.

Uncertainty in final diameter (U_{Df}),

$= \pm 0.001$ inch.

$$\text{Area } (A_f) = \frac{\pi D_f^{\,2}}{4}$$

$$= 0.01972 \text{ inch}^2$$

$$\frac{dA_f}{dD_f} = \frac{\pi D_f}{2}$$

$$= 0.2488$$

Uncertainty in final cross-sectional area,

$$U_{A_f} = \left[\left(\frac{dA_f}{dD_f} \cdot U_{D_f}\right)^2\right]^{\frac{1}{2}}$$

$$= 0.2488 \times 0.001$$

$$= 0.0002488$$

Uncertainty in %RA,

$$U_{\%RA} = \left[\left(\frac{\partial \%RA}{\partial A_i} \cdot U_{A_i}\right)^2 + \left(\frac{\partial \%RA}{\partial A_f} \cdot U_{A_f}\right)^2\right]^{\frac{1}{2}} \qquad \text{Equation A5}$$

$$\%\text{RA} = \left(\frac{A_i - A_f}{A_i}\right) \times 100$$

$$= \left(1 - \frac{A_f}{A_i}\right) \times 100$$

$$\frac{\partial \%RA}{\partial A_i} = \frac{100 A_f}{A_i^{\,2}}$$

$$= 811.36$$

$$\frac{\partial \%RA}{\partial A_f} = -\frac{100}{A_i}$$

$$= -2028.40$$

Now assigning all the calculated values in Equation A5, it is found that,

$$U_{\%RA} = \left[(811.36 * 0.000393)^2 + (-2028.40 * 0.0002488)^2\right]^{\frac{1}{2}}$$

$$= 0.597$$

One example of the use of the uncertainty analysis is shown in this section. This can be implemented to all experimental results discussed in this dissertation.

BIBLIOGRAPHY

[1] F. Venneri, et al., "Disposition of Nuclear Waste using Subcritical Accelerator-Driven Systems: Technology Choices and Implementation Scenarios", Nuclear Technology, Vol. 132, No. 1, pp. 15 (2000)

[2] Y. Dai, et al., "Mechanical Properties of Modified 9Cr-1Mo (T91) Irradiated at 6300C in SINQ Target-3", Journal of Nuclear Materials, Vol. 318, pp. 192-199, 2003

[3]T. Auger, et al., "Effect of contact conditions on embrittlement of T91 grade steel by lead-bismuth"Journal of Nuclear Materials, volume 335 Issue 2

[4] A.K.Roy, et al., "The role of Silicon Content on Environmental Degradation of T91 Steels" Journal of Material Engineering and Performance

[5] ASTM Designation E8-2004, "Standard test methods for tensile testing of metallic materials", American Society for Testing and Materials (ASTM) International

[6] Fast Track 8800, "Bluehill 2 Software," Instron Material Testing Systems

[7] Instron Testing Systems, "Specifications – Model 8862," Dynamic and Fatigue Test Systems – High Precision Electric Actuator Systems

[8] 25 MeV LINAC at Idaho Accelerator Center
http://iac.isu.edu/facilities/25MeV.html

[9] ASTM G5-94 (1999), "Standard Reference Test Method for Making Potentiostatic and Potentiodynamic Anodic Polarization Measurements," ASTM International

[10] ASTM G5-94 (1999), "Standard Reference Test Method for Making Potentiostatic and Potentiodynamic Anodic Polarization Measurements," ASTM International

[11] ASM Handbook, "Metallographic Techniques and Microstructures", Volume 9

[12] V. Raghavan, "Mechanical Properties," Chapter 5, Physical Metallurgy, pp. 164-165

[13-17] A. K. Roy, P. Kumar, D. Maitra, "Dynamic Strain Ageing of P91 Grade Steels of Varied Silicon Content," Materials Science and Engineering *A*, Vol. 499 (2009), pp. 379-386

[18,19] Pankaj, PhD dissertation, Effect of Temperature, Strain rate, and Silicon Content on Dynamic Strain Aging of modified 9cr-1Mo Steel. University of Nevada,Las Vegas, December 2007

[20] K. Shiba, et al.,in: Effects of Radiation on Materials: 17th International Symposium, ASTM STP 1270, Philadelphia, 1997, p. 753.

VITA

Graduate College
University of Nevada, Las Vegas

Hanumantha Rao Chava

Local Address:
4255 Tamarus st, apt#117
Las Vegas, NV, 89119

Degrees:
Bachelor of Engineering, 2004
Andhra University, Visakhapatnam

Thesis Title:
Temperature and Silicon Effects on Tensile and Corrosion Behavior of 9Cr-1Mo Steel

Thesis Examination Committee
Chairperson, Dr. Ajit Roy, Professor, Ph.D
Chairperson, Dr. Brendan O'Toole, Associate Professor, Ph.D
Committee Member, Dr. Anthony E. Hechanova, Associate Research Professor, Ph.D
Graduate Faculty Representative, Dr. Edward S. Neumann, Professor, Ph.D